Journal of Natural Gas Science and Engineering 94 (2021) 104127

Contents lists available at ScienceDirect

Journal of Natural Gas Science and Engineering

journal homepage: www.elsevier.com/locate/jngse

Modelling of the gas hydrate potential in Svalbard's fjords

Peter Betlem [a,b,*], Srikumar Roy [c], Thomas Birchall [a,b], Andrew Hodson [a,d], Riko Noormets [a], Miriam Römer [e], Ragnheid Skogseth [f], Kim Senger [a]

[a] Department of Arctic Geology, The University Centre in Svalbard, P.O. Box 156, N-9171 Longyearbyen, Svalbard, Norway
[b] Department of Geosciences, University of Oslo, Sem Sælands vei 1, 0371 Oslo, Norway
[c] Irish Centre for Research in Applied Geosciences (iCRAG), School of Earth Sciences, University College Dublin, Belfield, Dublin 4, Ireland
[d] Department of Environmental Sciences, Western Norway University of Applied Sciences, Røyrgata 6, N-6856 Sogndal, Norway
[e] MARUM - Center for Marine Environmental Sciences and Department of Geosciences, University of Bremen, Klagenfurter Str., DE-28359, Bremen, Germany
[f] Department of Arctic Geophysics, The University Centre in Svalbard, P.O. Box 156, N-9171 Longyearbyen, Svalbard, Norway

ARTICLE INFO

Keywords:
Gas hydrates
Arctic
Fjords
Flares
Modelling
Near-shore

ABSTRACT

Large amounts of methane are trapped as natural gas hydrate (NGH) in the sediments of the Arctic. Unlike NGH provinces offshore west of Svalbard (Vestnesa Ridge), NGH potential in Svalbard's fjords and near-shore environment is poorly constrained. In this study we modelled the NGH stability zone (GHSZ) to determine the NGH formation potential within the fjords of Svalbard. We applied a nearest neighbour interpolation method to dynamically derive statistical bottom-water temperature (BWT) trends from available CTD data. The BWT trends along with available geothermal gradient data constrained Svalbard-wide sub-bottom thermobaric models suitable for GHSZ modelling in the near subsurface. Analyses of source rock and fluid seepage data in Isfjorden, including 15 newly identified acoustic gas flares, indicate an active petroleum system with fluid migration reaching the seafloor with significant contributions of higher-order hydrocarbons to the gas feed. A GHSZ is predicted for most fjords at mean BWT conditions and 95:5 methane:ethane gas compositions. Suitable conditions for pure methane NGH formation are only met in the deepest parts of Isfjorden, Hinlopenstretet, Kross- and Kongsfjorden, and Rijpfjorden. Temporal constraints implemented along the well-defined Isfjorden transect indicated a notable negative response to water column warming. The predicted GHSZ across Svalbard's fjords is likely to disappear over the next few decades.

1. Introduction

Natural gas hydrates (NGHs) form where natural gas is present within the natural gas hydrate stability zone (GHSZ). The GHSZ is a dynamic zone governed by composition-specific thermobaric conditions (Sloan and Koh, 2007). NGHs are important as they represent a large sink of methane gas in sedimentary basins globally (Kvenvolden, 1998; Boswell and Collett, 2011; Milkov, 2004). Global GHSZ estimates are necessary to constrain uncertainties in NGH stability and occurrence (Minshull et al., 2020; Kvenvolden and Lorenson, 2001; Johnson, 2011) that are vital to accurately estimate hydrate-related resource (e.g., Max et al., 2005; House et al., 2006; Tohidi et al., 2010) and geohazard potential. Dissociating NGH have the potential to trigger submarine landslides (e.g., Ruppel and Kessler, 2017; Sultan et al., 2003), are seen as drilling hazards (e.g., McConnell et al., 2012), and may facilitate the release of methane into the atmosphere (e.g., James et al., 2016; Ruppel and Kessler, 2017). Atmospheric methane contributes to the global greenhouse effect, and further release is likely to affect the climate adversely (IPCC, 2014).

Polar NGHs may be particularly sensitive to climate change as enhanced global warming occurs through polar amplification. Warming-related polar NGH dissociation possibly results in a positive-feedback system (Fetterer et al., 2016; Marín-Moreno et al., 2013; James et al., 2016). Pan-Arctic NGH occurrence has mainly been predicted through coarse-scale, regional assessments relying on theoretical GHSZ conditions (e.g., Giustiniani et al., 2014; Tinivella and Giustiniani, 2016; Minshull et al., 2020, and references therein). Large-scale assessments favour the implementation of data with lower spatial resolution, generalised data trends, and simplified chemical compositions: local bathymetry (and hydrostatic pressure) are interpolated from low-resolution bathymetry charts; local thermal conditions are based on

* Corresponding author at: Department of Arctic Geology, The University Centre in Svalbard, P.O. Box 156, N-9171 Longyearbyen, Svalbard, Norway.
E-mail addresses: Peter.Betlem@unis.no (P. Betlem), Srikumar.Roy@icrag-centre.org (S. Roy), Thomas.Birchall@unis.no (T. Birchall), Andrew.Hodson@unis.no (A. Hodson), Riko.Noormets@unis.no (R. Noormets), MRoemer@marum.de (M. Römer), Ragnheid.Skogseth@unis.no (R. Skogseth), Kim.Senger@unis.no (K. Senger).

https://doi.org/10.1016/j.jngse.2021.104127
Received 15 April 2021; Received in revised form 9 June 2021; Accepted 1 July 2021
Available online 9 July 2021

global and regional bottom-water temperature (BWT) trends; and the presence of higher-order hydrocarbons is often omitted. Such simplifications rarely account for the complex conditions found throughout the Arctic (e.g., Marín-Moreno et al., 2013; Vadakkepuliyambatta et al., 2017; Ferré et al., 2020; Plaza-Faverola et al., 2017; Knies et al., 2015; Minshull et al., 2020). The effect of seasonal and short-term temperature fluctuations on submarine natural gas emissions remains largely unaddressed (e.g., Ferré et al., 2020; Marín-Moreno et al., 2013; Berndt et al., 2014).

The Svalbard archipelago, comprising all islands between 74 and 81° N and 10–35° E (Fig. 1), provides an opportunity to study the complexity and vulnerability of potential shallow-water, near-shore NGH provinces in a climate-sensitive area. Svalbard features higher-than-expected air temperatures given its latitude and offers laterally varying thermobaric and geological conditions (Ohm et al., 2019; Senger et al., 2019, and references therein). Svalbard's shallow waters feature large seasonal variability in water column temperatures (von Appen et al., 2016; Skogseth et al., 2020), possibly affecting hydrate stability.

Thermobaric modelling predicts NGH occurrence onshore Spitsbergen (Betlem et al., 2019; Minshull et al., 2020), and in Isfjorden, Spitsbergen's largest fjord system (Roy et al., 2012; Betlem, 2018), though to date no discoveries of NGH have been reported in Svalbard. Recent studies have identified temporal and spatial variations in the permanently methane-supersaturated water column (Damm et al., 2021), numerous (active) seeps and more than 1300 pockmarks (e.g., Roy et al., 2015, 2016, 2019; Ferré et al., 2020; Ćwiąkała et al., 2018) in Isfjorden. Given the shallow fjord depths and (local) methane-supersaturation in the water column, natural gases and dissociated methane hydrate may migrate directly into the atmosphere (Ruppel and Kessler, 2017; Berndt et al., 2014; Damm et al., 2021).

We here model the gas hydrate stability zone (GHSZ) for the fjords around Svalbard and investigate Svalbard's near-shore NGH potential. We implement high-resolution bathymetry, regional conductivity–temperature–depth (CTD) data of the water column, and chemical compositions constrained by published offshore and onshore hydrocarbon composition analyses. We further evaluate the potential of NGH occurrence by looking at potential reservoir rocks and migration pathways in proximity of the modelled GHSZ. We then use insights from onshore Svalbard to pinpoint areas of high potential suitable for future investigations and surveying. Finally, we assess the impact of water column warming through a well-calibrated cross-section in Isfjorden based on water column temperature changes over the last few decades.

1.1. Geological and physiographic setting: exploring for NGH ingredients

Svalbard's geological record comprises an almost complete succession from the Pre-Ordovician basement and Devonian Red sandstones to the Palaeogene basin-infill of the Central Spitsbergen Basin (CSB). The succession offers multiple organic-rich source rocks and porous reservoir rocks (Henriksen et al., 2011b; Worsley, 2008; Dallmann et al., 2015). The Svalbard archipelago is routinely used as an analogue for petroleum plays targeted in the south-western Barents Sea (Henriksen et al., 2011b). The presence of a functional petroleum system has been indicated by hydrocarbon shows and technical discoveries in several wildcat exploration wells onshore (Senger et al., 2019), an unconventional discovery of shale gas in research wells in Adventdalen (Ohm et al., 2019), by hydrocarbons in numerous outcropping sedimentary rocks (e.g., Abay et al., 2017), by active oil and gas seeps, and pockmarks (e.g., Roy et al., 2019, and references therein; Senger et al., 2019; Liira et al., 2019; Knies et al., 2004). Notably, at least one petroleum exploration well in inner Billefjorden is classified as a technical oil and gas discovery (Senger et al., 2019; Verba, 2007, 2013), and natural gas is present beneath the permafrost across large parts of Svalbard.

Mature organic source rocks are widespread, with examples including Palaeozoic, Mesozoic, and Cenozoic coals in addition to Palaeozoic and Mesozoic organic-rich shales (e.g., Nøttvedt et al., 1993; Paech and Koch, 2001; Nicolaisen et al., 2019; Steel et al., 1981; Harland et al., 1976; Blumenberg et al., 2018). The shale-dominated Middle Triassic Botneheia Formation and Middle Jurassic to Lower Cretaceous Agardhfjellet Formation are well known as onshore counterparts to prolific source rocks in the Barents Sea (Nøttvedt et al., 1993; Abay et al., 2014, 2017; Bjorøy et al., 2010; Koevoets et al., 2016; Ohm et al., 2019; Mørk and Bjorøy, 1984; Abay et al., 2014).

Evidence of faulting (e.g., Billefjorden Fault Zone; BFZ) is widespread throughout the archipelago (e.g., Harland et al., 1974; Lowell, 1972). Western and central Spitsbergen has been affected by structural shortening during the formation of the West Spitsbergen Fold-and-thrust Belt in the Palaeogene. Elsewhere, Spitsbergen has been affected by earlier major rifting and orogenies (Henriksen et al., 2011b). These events have resulted in deep burial and subsequent uplift, extensive fracturing and other structural heterogeneities that may compromise the top seal integrity and facilitate fluid migration and leakage (Ogata et al., 2014). Major uplift occurred in several events across the Barents Shelf throughout the Cenozoic (e.g., Lasabuda et al., 2018), with up to 3 km of uplift occurring on Svalbard (Henriksen et al., 2011a). Uplift related to the glacial cycles of the past few million years is perhaps responsible for the most significant and on-going hydrocarbon remigration (Ohm et al., 2008), erosion, and out-of-equilibrium pressure conditions (e.g., Birchall et al., 2020; Wallmann et al., 2018; Westbrook et al., 2009; Serov et al., 2017; Himmler et al., 2019; Roy et al., 2016).

Thousands of pockmarks have been documented in Svalbard's fjords and straits. The latter include Kongsfjorden (Streuff, 2013), Van Keulenfjorden (Kempf et al., 2013; Forwick et al., 2009), Hornsund (Ćwiąkała et al., 2018), Isfjorden (including inner fjords) (Roy et al., 2015, 2016; Baeten et al., 2010; Forwick et al., 2009), Forlandsundet (Portnov et al., 2016; Butschek et al., 2019), possibly Lomfjorden (Streuff et al., 2017), and Magdalenefjorden (Streuff et al., 2018). Geochemical analyses of hydrocarbon anomalies in the water column and near-surface marine sediments indicate a mixture of biogenic and thermogenic signatures (Knies et al., 2004; Liira et al., 2019) and complex lateral and vertical methane transport in the entire water column (Damm et al., 2005). Parts of Isfjorden remain permanently supersaturated with pronounced temporal and spatial variations in methane excess levels (Damm et al., 2021).

The formation and distribution of pockmarks has been related to the possible dissociation of NGHs, seepage of shallow gas, permeable fluid migration pathways, tectonic fault and igneous conduits, external trigger mechanisms such as seismic activity, and dewatering of soft sediment due to deposition of debris lobes (Roy et al., 2015, 2019, and references therein). Gas flares have been documented in Kross- and Kongsfjorden (Bohrmann, 2015), Isfjorden (Bohrmann, 2015; Roy et al., 2019), at Vestnesa ridge (e.g., Ferré et al., 2020, and references therein), at the shelf off Prins Karls Forland (Sahling et al., 2014; Westbrook et al., 2009) and along the entire continental margin west of Svalbard to Bjørnøya in the south (Mau et al., 2017). The Hornsund Fracture Zone has been suggested as a potential migration pathway for thermogenic (possibly through hydrate intermediary) methane (Damm et al., 2005).

Major ocean currents affect offshore (Onarheim et al., 2014; Tverberg et al., 2019) and onshore thermal conditions across Svalbard (e.g., Przybylak et al., 2014). Several fjords, including Isfjorden, penetrate deep into the interior of Svalbard's largest island, Spitsbergen. They expose inner Spitsbergen to the effects of the warm and saline Atlantic water, advected northward by the West Spitsbergen Current (WSC) (Cottier et al., 2007; Nilsen et al., 2008, 2016; Luckman et al., 2015). In the east, colder Arctic type water is carried by the East Spitsbergen Current (ESC), part of which also continues northward up the west coast of Spitsbergen as the Spitsbergen Polar Current (SPC) (Maciejowski and

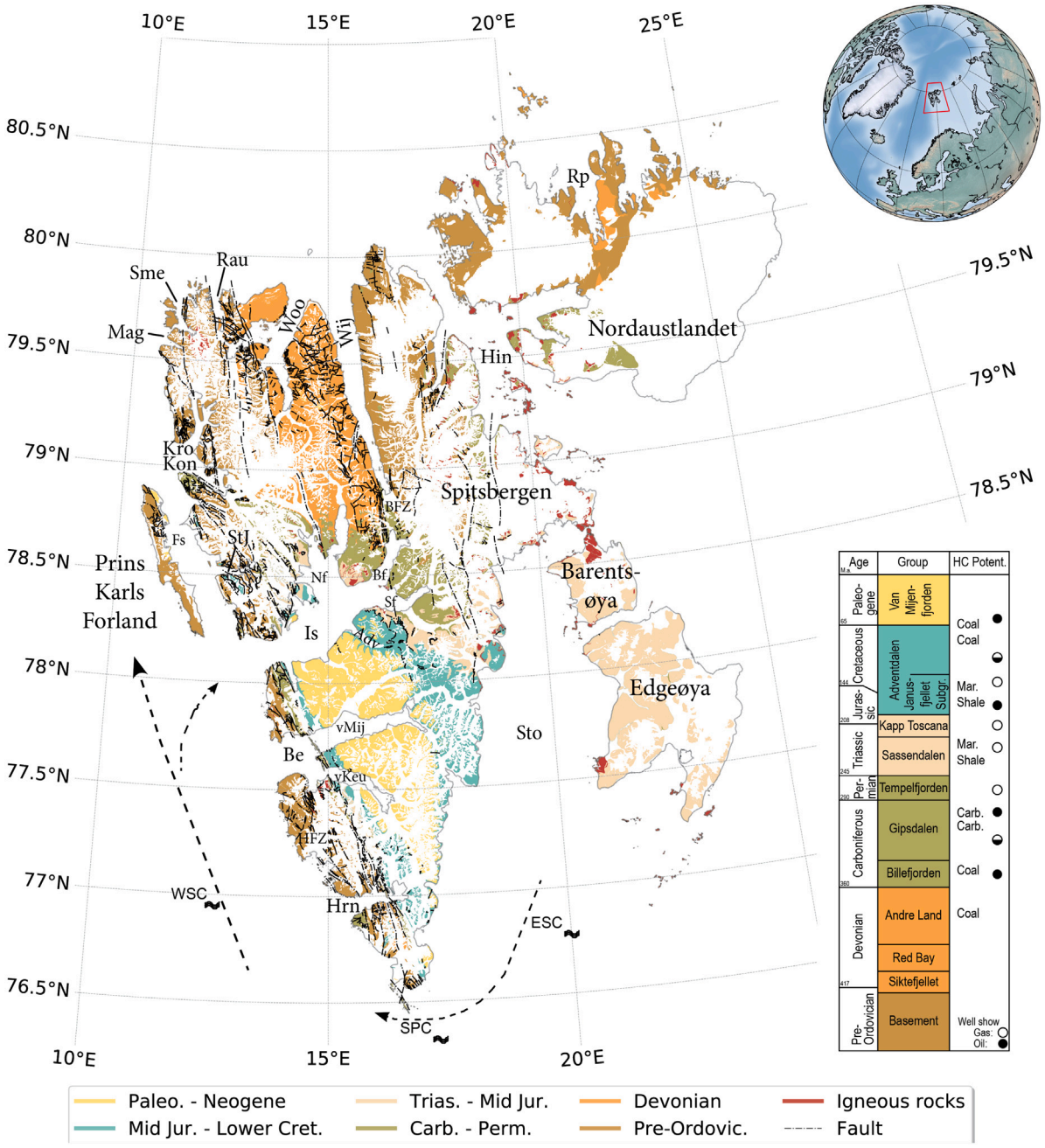

Fig. 1. The bedrock geology map of Svalbard. The stratigraphic log is based on an unpublished figure by Arild Andresen (University of Oslo), further updated with source rocks and hydrocarbon potential (HC Potent.) summarised in the main text. Geoscientific data courtesy Norwegian Polar Institute (Dallmann et al., 2015). Adv, Adventdalen; Be, Bellsund; Bf: Billefjorden; BFZ, Billefjorden Fault Zone; CSB, Central Spitsbergen Basin; ESC, East Spitsbergen Current; Fs, Forlandsundet; Hin, Hinlopenstretet; HFZ, Hornsund Fault Zone; Hrn, Hornsund; Is, Isfjorden; Kon, Kongsfjorden; Kro, Krossfjorden; Mag, Magdalenefjorden; Nf, Nordfjorden; Rau, Raudfjorden; Rp, Rijpfjorden; Sf: Sassenfjorden; SPC, Spitsbergen Polar Current; Sme, Smeerenburgfjorden; StJ, St Jonsfjorden; Sto, Storfjorden; vKeu, Van Keulenfjorden; vMij, Van Mijenfjorden; Wij, Wijdefjorden; Woo, Woodfjorden; WSC, West Spitsbergen Current. EPSG:32633 used as CRS.

Michniewski, 2007; Fraser et al., 2018; Nilsen et al., 2016; Tverberg et al., 2019; Skogseth et al., 2020). The inner fjords and eastern waters (e.g., Hinlopenstretet, Rijpfjorden, Storfjorden) regularly freeze over with sea ice in winter that sometimes lasts into summer and beyond (e.g., Skogseth et al., 2004; Onarheim et al., 2014; Isaksen et al., 2016; Muckenhuber et al., 2016). Here, like in other Arctic coastal environments, temporal variability in BWTs is further complicated by factors that include the effects of water-terminating glaciers, sea ice formation, and potentially (relic) subsea permafrost (Ruppel and Kessler, 2017; Vadakkepuliyambatta et al., 2017; Ferré et al., 2020; Marín-Moreno et al., 2013). Water column temperatures range from freezing point (−1.9 °C) to upper single-digit centigrade (Cottier et al., 2010; Promińska et al., 2018; Tverberg et al., 2019; Skogseth et al., 2019, 2020), though variability is highest close to the water surface.

Long term mean annual surface air temperatures vary between −3 °C and −10 °C over just a few tens of kilometres, with glacial cover and permafrost featuring their greatest extent towards the north east. Onshore, annual temperatures have risen by 0.9 °C and 1.6 °C per decade in summer and winter, respectively, for the 1971–2017 period. Ongoing warming affects slope stability and contributes to thawing permafrost (Nordli et al., 2014; Hanssen-Bauer et al., 2019). Decadal water column thermal trends already indicate advective heat transfer into the fjord waters around Svalbard (Skogseth et al., 2020; Pavlov et al., 2013; Promińska et al., 2018), and further heat-propagation into

Table 1
Overview of all available datasets integrated in this study. Herein: CTD, conductivity–temperature–depth; MBES, multibeam echosounder.

Data type	Location/extent	Comments	Source
Regional databases			
Bathymetry and MBES	All fjords	200 m resolution, locally 5 m	Jakobsson et al. (2020), Norwegian Mapping Authority: permission no. 13/G706, the University Centre in Svalbard (UNIS)
Geological maps	Onshore Svalbard and Isfjorden	Mapped at 1:100000 scale in most areas, at 1:250000 in east Svalbard	Norwegian Polar Institute, NPI (2016)
CTD data	All fjords		Skogseth et al. (2019), this study (Table 4, included in Appendix A)
Boreholes and dataloggers			
Petroleum exploration boreholes	18 sites onshore Svalbard	Temperature and lithology control	UNIS, Betlem et al. (2018), Midttømme et al. (2015), Senger et al. (2019)
Research boreholes	8 wells in Adventdalen	Full coring, wireline logs, chemical and gas analysis	Braathen et al. (2012), Elvebakk (2010), Huq et al. (2017), Ohm et al. (2019), Olaussen et al. (2019)
Geochemical sampling (onshore)	Adventdalen pingos	Chemical composition	Hodson et al. (2019), Yoshikawa and Harada (1995), Yoshikawa (1998)
Geochemical sampling (offshore)	Isfjorden, Krossfjorden, Kongsfjorden, Van Mijenfjorden, Bellsund, Hornsund, Storfjorden	Chemical composition	Knies et al. (2004), Liira et al. (2019), Weniger et al. (2019)
Geophysical datasets			
Seismic (2D)	Most fjords and onshore		Norsk Hydro, Equinor, Svalex, University in Bergen, UNIS, Bælum and Braathen (2012), Bælum et al. (2012), Blinova et al. (2012), Eiken (1985), Mjelde (2005), Roy et al. (2014), Roy et al. (2019), Senger et al. (2013)

the sediments is likely (Ferré et al., 2012; Vadakkepuliyambatta et al., 2017). An increased inflow of Atlantic Water in Isfjorden is linked to an increase in mean fjord temperatures of 0.7 °C per decade in winter and 0.6 °C per decade in summer. This coincides with a slight increase in salinity levels over the 1987–2017 period (Skogseth et al., 2020).

Exploration borehole data (Fig. 3B) (Midttømme et al., 2015; Betlem et al., 2018), xenoliths from Quaternary volcanism at Bockfjorden (Banks et al., 1998), and hot springs around Svalbard (e.g., Salvigsen and Elgersma, 1985; Reigstad et al., 2011) suggest above-average heat flow values (Amundsen et al., 1988). Pan-archipelago geothermal gradient measurements generally fall within the 25 to 40 ° C/km range (33 °C/km on average) (Betlem et al., 2018, 2019). Local geothermal gradients may be as high as 79 °C/km (e.g., Bockfjorden and Trollkjeldene hot springs; Amundsen et al., 1988; Banks et al., 1998; Hoel and Holtedahl, 1911).

2. Methods and data

We integrated all relevant data (Table 1) to calculate the GHSZ extent and thickness for the fjords around Svalbard building upon the workflow presented by Betlem et al. (2019). The workflow implements structure-I gas hydrate phase boundary curves generated through the Heriot Watt University thermodynamic hydrate (HWHydrate) model as described by Tohidi et al. (1995) and Masoudi et al. (2004). HWHydrate implements the Valderrama modification of the Patel and Teja equation of state (VPT EoS) (Valderrama, 1990), non-density dependent mixing rules for polar–nonpolar and polar–polar interactions (Avlonitis et al., 1994), and the Parrish (1972) implementation of the solid solution theory of Van Der Waals (1959). The Kihara model for spherical molecules accounts for the effect of guest compounds in the hydrate phase (Kihara, 1953). Salts, the only inhibitors used in this study, are implemented as pseudo-components with defined critical properties and acentric factors in a modified VPT EoS (Masoudi et al., 2004).

Chemo-thermo-baric condition input was as complex as the data allowed, although bathymetric and computational efficiency limited modelling cell sizes to 200 × 200 × 25 m for each of the fjords (i.e., the subsurface grid). The subsurface grid followed a 200 × 200 × 0.1 m surface layer that functioned as an input layer for bottom-water conditions and followed fjord bathymetry derived from IBCAOv4 data (Jakobsson et al., 2020), itself featuring a 200 × 200 m grid resolution (Fig. 3A). The centre points of each cell in the surface layer were defined as grid point surface nodes.

Seafloor thermal regimes were dynamically calculated (Fig. 2) using all CTD data from the UNIS Hydrographic Database (UNIS HD, Skogseth et al., 2019) and combined with additional unpublished data sets available for Isfjorden, Kongsfjorden, and Rijpfjorden (Table 4, included in Appendix A). CTD data originating from the UNIS HD were metadata filtered by their quality key (“Good”). Points beyond the fjord outlines and specific date–time intervals were removed. CTD data with greatest depths differing by more than 25 m compared to the respective bathymetry depths were rejected, as depicted by the blue “1” entry in Fig. 2.

We applied dynamic lateral and vertical binning for the calculation of synthetic temperature profiles to overcome the loss of depth-related BWT variations. At each grid point surface node, all CTD data within given a range were selected through use of the SciPy (Virtanen et al., 2020) spatial cKDTree nearest neighbour (NN) search algorithm. Data that fit both the NN zone and quality criteria were used as input for the calculation of 10th, 50th and 90th percentile synthetic CTD profiles for each grid point (Fig. 2). First, all accepted CTD data within a radius were selected (schematically shown in Fig. 2A, red entries “2–5”) and binned at 5 m intervals from sea level to greatest CTD depth. The Kongsfjorden and Hinlopenstretet study areas implemented an NN range of 10 km, with the remaining study areas implementing a range of 5 km. Equal weights were applied to all CTD data within range. 10th, 50th and 90th percentile temperature values were then calculated for each binned depth and stored in node-specific 10th, 50th and 90th percentile synthetic temperature profile. Percentiles were calculated through use of the pandas Python-package quantile function, with the “linear” interpolation mode enabled (McKinney, 2011). Finally, the node-specific synthetic temperature profiles were queried with node-specific bathymetries to obtain the corresponding seafloor temperature models (p10-T, p50-T, p90-T) at each grid point surface node (Fig. 2B). The median p50-T seafloor temperature model functioned as the base case scenario and the p10-T and p90-T models as end-member scenarios for BWT variability.

Where sufficient data were available, temporal change was implemented for 2D transects by constraining the CTD data with specific date–time intervals to assess seasonal, annual and decadal dynamics. CTD data collected beyond these intervals were rejected for those

Table 2
Overview of the six scenarios employed in this study along with the associated input parameters. Herein B and E resemble the thermal base case for respectively a pure methane and 95:5 Me:Et hydrocarbon composition. *BWT profile* indicates which of the statistical BWT temperature trends is applied to obtain the BWT at the grid point surface node.

Scenario	BWT profile	Methane fraction	Ethane fraction	Salinity (ppt)	Pressure	Geothermal gradient (°C/km)
A	p10-T	0.95	0.05	35	Hydrostatic	33
B	p50-T	0.95	0.05	35	Hydrostatic	33
C	p90-T	0.95	0.05	35	Hydrostatic	33
D	p10-T	1	0	35	Hydrostatic	33
E	p50-T	1	0	35	Hydrostatic	33
F	p90-T	1	0	35	Hydrostatic	33

specific calculations. Accurate implementation of BWT trends along the well-defined Isfjorden transect through 20 multi-year CTD data clusters followed the definition of seasons as per Skogseth et al. (2020). Winter was defined around the seasonal sea ice low of March, i.e., January through May, summer as July through the end of September. Seasonal water column temperatures (50th percentile) for the decades spanning 2000–2009, 2010–2019 and 2020–2029 were calculated through use of the NN approach (radius = 500 m) at 50 m intervals along the cross-section connecting each of the CTD cluster locations. The 2020–2029 prediction implemented an additional warming of 0.7 and 0.6 °C per decade warming for winter and summer, respectively (Skogseth et al., 2020).

Subsurface geothermal conditions were extrapolated from the grid point surface node using averaged archipelago-wide steady-state geothermal gradients (33 °C/km; Fig. 3B) (e.g., Betlem et al., 2019, 2018; Midttømme et al., 2015).

Chemical compositions were mainly derived from hydrocarbon sampling surveys (e.g. Liira et al., 2019, and references therein; Knies et al., 2004; Weniger et al., 2019) within the fjords (Fig. 3C) and from petroleum exploration boreholes (e.g., Huq et al., 2017; Ohm et al., 2019; Verba, 2007, 2013; Senger et al., 2019; Shkola, 1977), and constrained the hydrocarbon composition used for modelling. Two hydrocarbon compositions were taken to investigate the GHSZ extent, being 100:0 pure methane and 95:5 methane-to-ethane (Me:Et). Given only minor variations in bottom-water salinities were observed in CTD data, water column and pore-water salinities were kept constant at 35 ppt for chemo-baric calculations (i.e., NGH phase boundary and subsurface pressure regime). This gave rise to the six modelling scenarios employed in this study (Table 2).

Additional water column and marine geology information was acquired as part of cruise HE-449 on research vessel R/V Heincke in August 2015 (Römer and Mau, 2015). The findings supplement existing knowledge on pockmarks, shallow gas trapped in glacial sediments, and acoustic flares in Isfjorden (Roy et al., 2019, 2014, 2016, 2015). R/V Heincke is equipped with a Kongsberg EM710 multibeam echosounder operating at frequencies of 70–100 kHz that allowed for the detection of such high backscatter anomalies as those caused by gas bubbles, i.e., flares. Water column records were analysed using QPS Fledermaus tools and the FMMidwater module, using the FMGeopickingTool to extract the flare source point data as point data (Table 5, included in Appendix A).

The integrated analysis of key geotransect seismic data implements the transect described by Blinova et al. (2012). Inclusion of the modelled GHSZ data implemented the time-depth conversion using v = 1470 m/s and v = 4000 m/s for the water column and compacted sediments (e.g., Bælum and Braathen, 2012; Elverhoi and Gronlie, 1981; Blinova et al., 2012), respectively.

Table 3
Key GHSZ modelling results for Svalbard's modelled fjords (overall) and Isfjorden. Table 2 provides the input parameters for the six distinct scenarios A–F.

Location	Scenario	Max upper boundary depth (mbsl)	Max lower boundary depth (mbsl)	Lateral extent (%)	Figure
Overall	A	125	350	10.4	Fig. 5A
Overall	B	125	350	4.6	Fig. 5B
Overall	C	0	250	1.4	Fig. 5C
Overall	D	125	350	6.8	Fig. 5D
Overall	E	50	250	2.6	Fig. 5E
Overall	F	0	250	0.5	Fig. 5F
Isfjorden	A	125	350	28.8	Fig. 6A
Isfjorden	B	125	350	14.9	Fig. 6B
Isfjorden	C	100	350	7.4	Fig. 6C
Isfjorden	D	25	250	3.6	Fig. 6D
Isfjorden	E	0	225	2.6	Fig. 6E
Isfjorden	F	0	225	0.8	Fig. 6F

3. Results

Table 3 provides the cumulative results of all study areas for the six scenarios (A–F) listed in Table 2. These also cover the Isfjorden study, which forms a data-rich case study that may help address findings in the other study areas. An extended version of Table 3 covers the remaining fjords and is included as an electronic supplement (Table 6, included in Appendix A). The electronic supplement also includes zoom-ins covering the fjords that feature a predicted GHSZ, along with the locations of tributary fjords mentioned in the main text.

CTD data density and bottom-water temperature trends

The grid point-dependent water column temperature (10th, 50th, 90th percentile) profiles resulted in the BWT (p10-T, p50-T and p90-T) models shown in Fig. 4. Each BWT model featured empty patches where data scarcity was indicated by low (and even zero) CTD-point density areas in Fig. 3B. Parts of the inner fjords and shallows were mainly affected by an insufficient spatial cover, as indicated by low CTD data density. CTD data coverage was greatest for the fjords where a 5 km NN radius was employed. Coverage ranges from 100% for Magdalenefjorden and Hornsund to 85% for Rijpfjorden. Lower values were observed for Hinlopenstretet (81%) and Storfjorden (91%) even while implementing a wider 10 km NN range. Low data coverage was most notable for the southern part of Hinlopenstretet, and the most northern part of Storfjorden. Minor gaps were furthermore observed near 19.5 ° E and 78.2 ° N in Storfjorden.

Across the study areas, the lowest modelled BWTs corresponded with the freezing point of saline water (−1.9 °C, 35 ppt salinity). Thermal lows were observed near glacier fronts and at shallower and/or barricaded inner fjords, as seen at barrier-forming islands of Akseløya and Mariaholmen (see also Høyland, 2009; Skarðhamar and Svendsen, 2010). Rijpfjorden and Storfjorden feature colder depth-temperature trends. Mean values for the p10-T, p50-T and p90-T models all fall within a 0 +− 1.3 °C range. The western fjords feature considerably higher variations, as seen for Isfjorden (mean p10-T: 0 °C, mean p50-T: 1.6 °C, mean p90-T: 3.1 °C) and Kongsfjorden-Krossfjorden (0.5, 2.2, 3.5 °C). Thermal regimes in the west are warmer. Maxima in the implemented raw data locally pass 8 °C in Bellsund and 7 °C in Isfjorden, compared to maxima of 5.4 °C in Rijpfjorden and 4.4 °C in Storfjorden.

3.1. GHSZ in Svalbard's fjords

Six scenarios were modelled to predict the GHSZ extent and thickness in Svalbard's fjords (Fig. 5). With the exception of Bellsund, Magdalenefjorden and St. Jonsfjorden, the models predicted NGH stability for all fjords under at least the most favourable scenarios (p10-T thermal and 95:5 Me:Et conditions). At base case p50-T thermal conditions

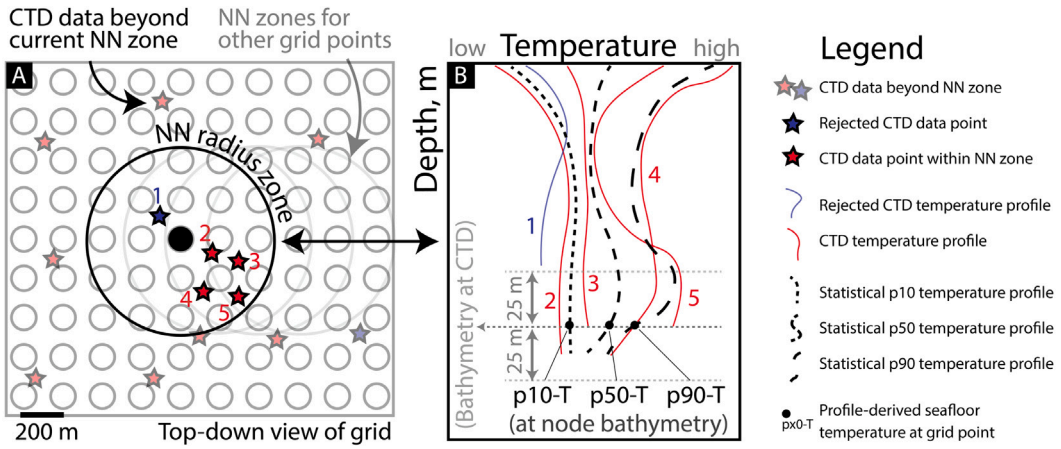

Fig. 2. Nearest neighbour (NN) approach for calculating BWTs at each of the grid point surface nodes. CTD data points beyond the NN zone (numberless stars, A) are ignored in the calculation (B), as are points that are rejected on grounds discussed in the text (star 1). CTD data that fit both the NN zone and other constraints (stars 2–5) are binned and used to calculate 10th, 50th, and 90th percentile temperature profiles. Grid point node temperatures (p10-T, p50-T, p90-T) are then retrieved from these statistical profiles at the corresponding grid point node depth. This is repeated for all grid point surface nodes in the grid.

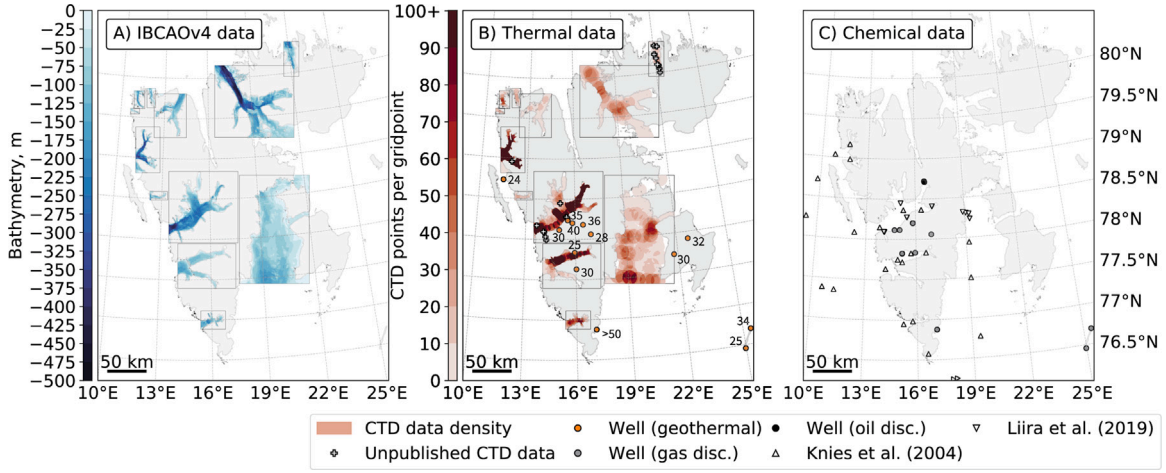

Fig. 3. Overview of key input data. (A) Overview of available bathymetry (Jakobsson et al., 2020) within the study areas. Approximate geothermal gradient estimates given in (B) are in ° C/km (Midttømme et al., 2015; Betlem et al., 2018). CTD data density is based on a combination of the UNIS Hydrographic database (Skogseth et al., 2019) and unpublished data (Table 4, included in Appendix A). (C) Hydrocarbon shows in boreholes from Senger et al. (2019). Maps implement EPSG:32633 as the CRS.

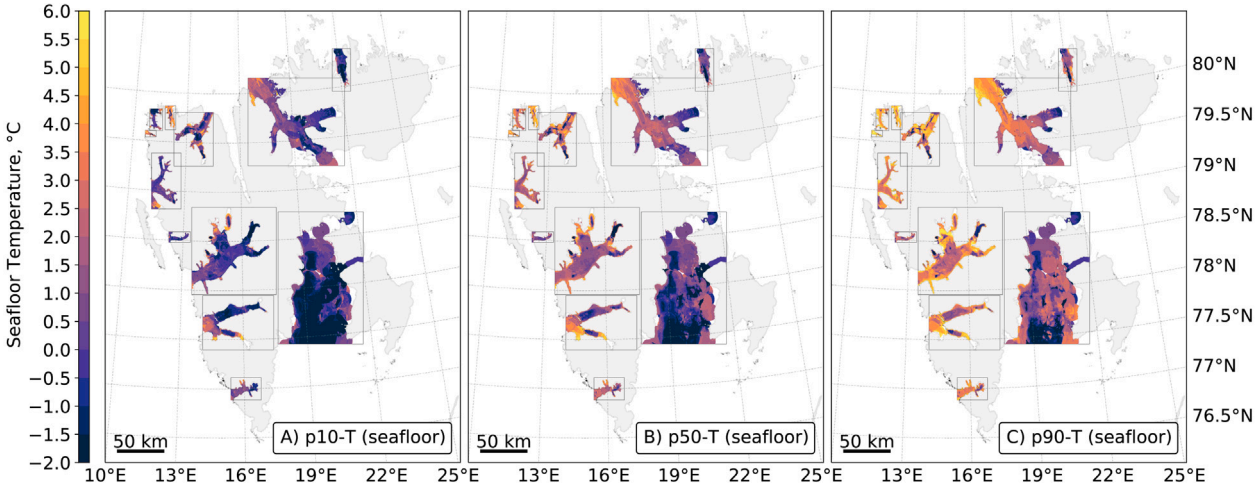

Fig. 4. Modelled temperatures of the fjords based on the 10th, 50th, and 90th percentile temperature profiles calculated at each surface grid point node. Maps implement EPSG:32633 as the CRS.

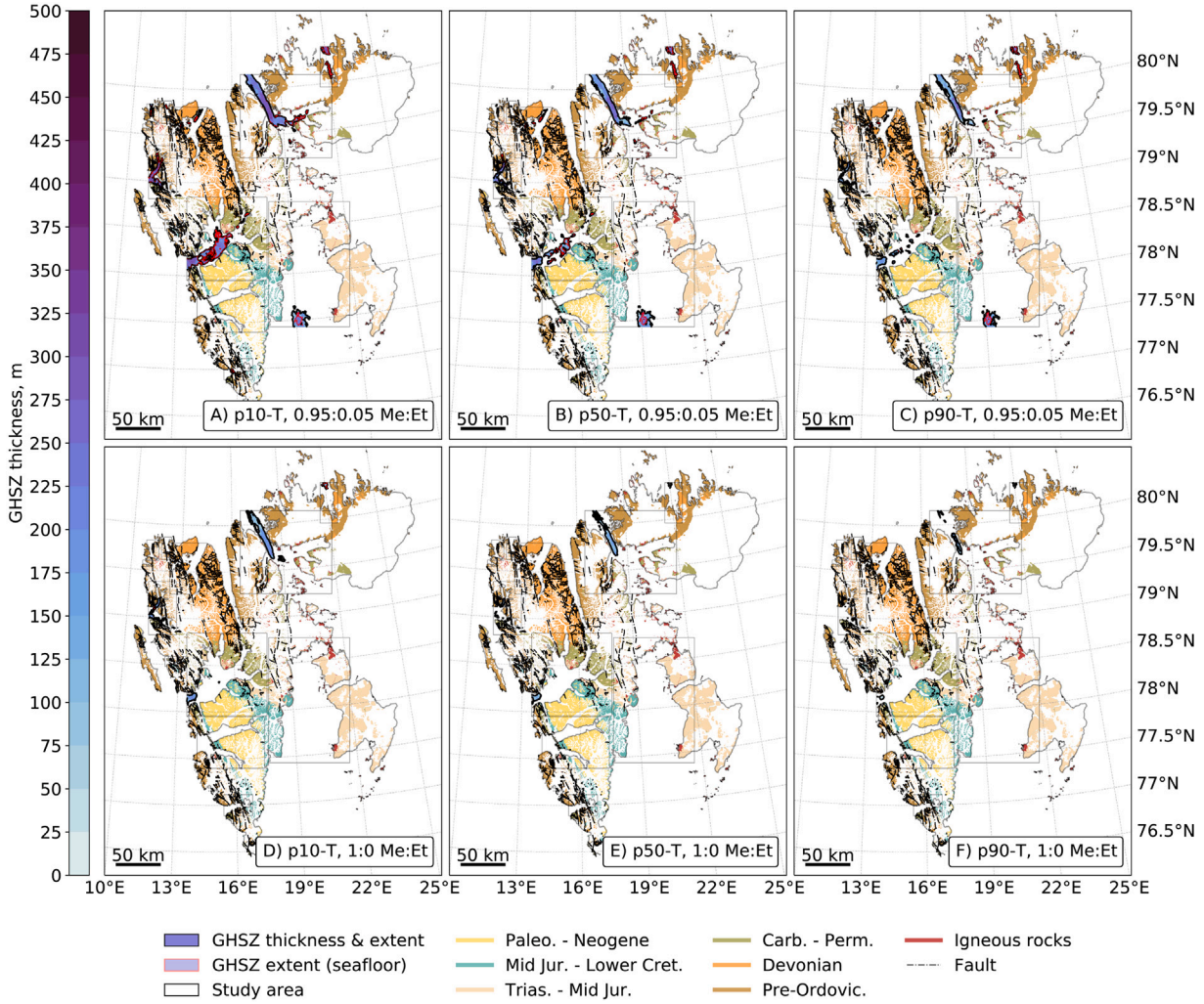

Fig. 5. Predicted GHSZ extent and thickness for the studied fjords around Svalbard. Throughout this figure and the next, temperature increases towards the right, and pure methane and 95:5 Me:Et scenarios are split horizontally. Geoscientific data courtesy Norwegian Polar Institute (Dallmann et al., 2015). Maps implement EPSG:32633 as the CRS.

NGH-stable regimes were predicted for Hinlopenstretet (Table 6; B: 95:5 Me:Et, E: 100:0 Me:Et), Isfjorden (B, E), Kongsfjorden-Krossfjorden (B, E), Raudfjorden (B), Rijpfjorden (B, E), Smeerenburgfjorden (B), Storfjorden (B) and Woodfjorden (B). Overall lateral extent varied between 4.6% fjords extent for 95:5 Me:Et conditions and 2.6% for 100:0 Me:Et conditions. Maximum GHSZ thicknesses of up to 350 m and 250 m were predicted, respectively.

Strong variations in the predicted GHSZ extent are observed between the different BWT models. For the Kongsfjorden-Krossfjorden area the p10-T thermal conditions give rise to 31.7% (Kongsfjorden A) lateral cover versus only 0.2% for the p90-T thermal conditions (Kongsfjorden F). Implementation of the p10-T thermal and 95:5 Me:Et conditions (Table 6; Overall A) led to calculated GHSZ thicknesses of up to 350 m down from the seafloor. As much as 10.4% of the lateral extent of the total modelled fjord area was predicted to be hydrate-stable.

In general, p10-T BWT trends resulted in the largest modelled GHSZ extent (A, D), which was further enlarged by the presence of higher order hydrocarbons (A). Smaller extents were predicted for the scenarios featuring pure methane compositions (D–F) and p90-T BWT conditions (C, F). Only the deepest parts of Isfjorden, Kongsfjorden-Krossfjorden, Hinlopenstretet, and Rijpfjorden featured NGH stable domains when implementing both (F). For all areas the GHSZ retreat was paired with thinning and dispersion.

Irrespective of the model scenario, the predicted GHSZ was thickest in the deepest parts of the fjords (>200 m depth) and thinnest towards the coast. Towards the outer rim of the zone's spatial extent in thick-to-thin GHSZ transects, the upper boundary of the GHSZ sometimes deflected downward and away from the seafloor by as much as 125 m. Zones with deflected upper boundaries were most pronounced for the scenarios in which the GHSZ was at its thickest and greatest lateral extent (A–C). Boundary deflection reduced in prominence for warmer and pure methane scenarios (F).

3.1.1. *Isfjorden*

The predicted GHSZ for Isfjorden (Fig. 6) shows that the deep basin at the mouth of Isfjorden consistently featured the thickest parts of the GHSZ, corresponding to the deepest section of the fjord. Water depths exceeding 400 m generated GHSZ thicknesses ranging from 350 m (A) to less than 100 m (F). Normalised lateral extent varied between 28.8% for the p10-T thermal and 95:5 Me:Et conditions (A) and 0.8% for p90-T thermal and 100:0 Me:Et conditions (F). In comparison, the p50-T base case condition scenarios gave rise to normalised lateral extents of 14.9% (B) and 2.6% (E), respectively.

For the three 95:5 Me:Et scenarios (Fig. 6A–C), the GHSZ is predicted to extend into inner Isfjorden. The GHSZ covers outcropping strata ranging in age from the Palaeogene to Carboniferous and covers several organic-rich sequences that include the shale-dominated Agardhfjellet Formation associated with shale gas in Adventdalen and in the Tromsøbreen petroleum exploration well (Ohm et al., 2019). Major faults, which may act as potential fluid migration pathways and

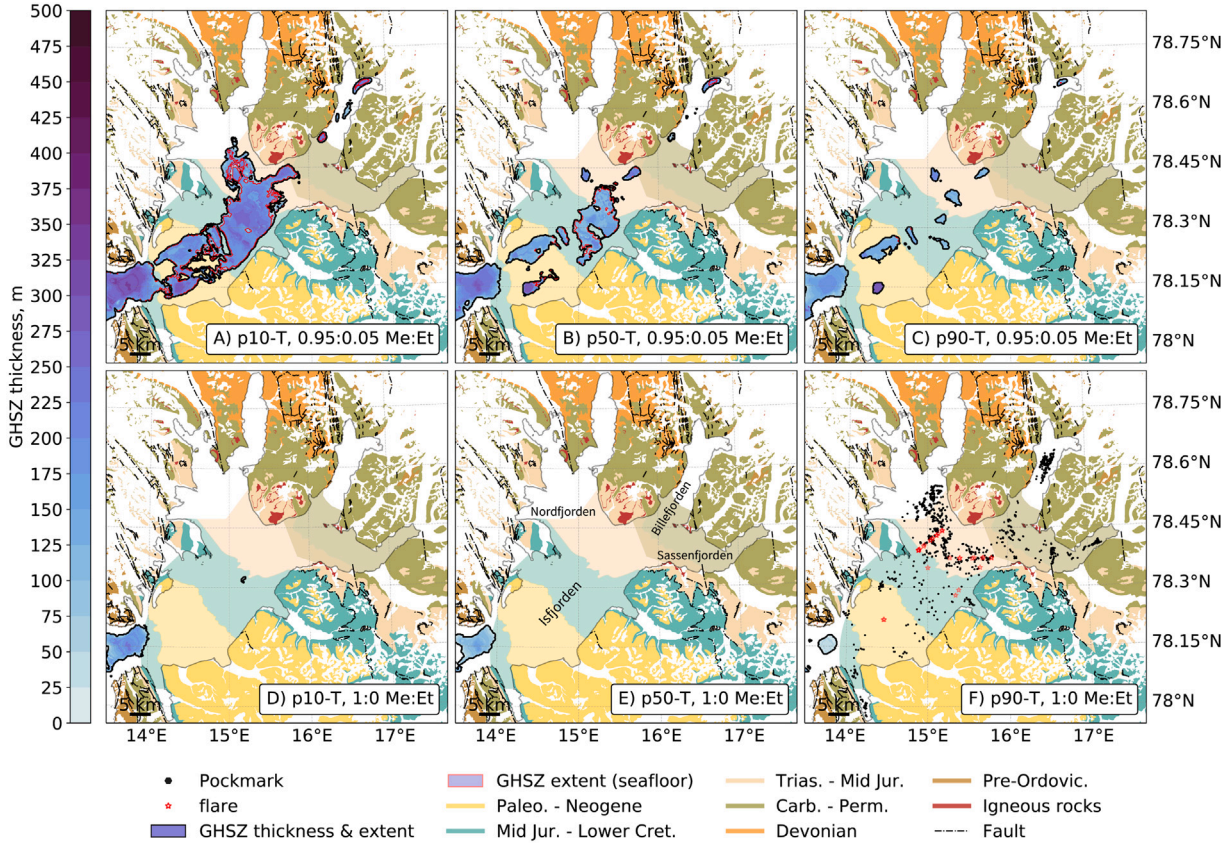

Fig. 6. Predicted GHSZ thickness and extent for Isfjorden. Seepage features (i.e., pockmarks, flares) are only plotted in (F) for clarity purpose. Geoscientific data courtesy Norwegian Polar Institute (Dallmann et al., 2015) and Blinova et al. (2012). Maps implement EPSG:32633 as the CRS.

are closely associated with dense pockmark clusters (Roy et al., 2019, 2015), intersect with the GHSZ (Fig. 6).

The predicted GHSZ implementing the p10-T low-temperature end-member case scenario and 95:5 Me:Et conditions (A) covers 409 of the 1304 known pockmarks and 21 of the 33 identified flare sites in Isfjorden. These include the eleven flares newly identified along the two key transects (Table 5, included in Appendix A). Dispersed pockets of NGH stability are predicted to occur in inner Billefjorden in proximity to the minor oil discovery reported from a coal exploration borehole. The dispersed pockets increase in thickness towards Adolfbukta. Parts of these pockets are predicted to remain stable under p50-T and p90-T 95:5 Me:Et configurations (B, C). The implementation of p50-T and p90-T thermal conditions resulted in a retreat of the modelled GHSZ to a dispersed corridor along the SW-NE axis. The lateral extent was limited to 14.9% and 7.4% of the fjord, respectively. The amount of upper boundary deflection decreased simultaneously, with next to no bulging noticeable for the p90-T 95:5 Me:Et scenario.

The three scenarios implementing 100:0 Me:Et compositions saw the calculated GHSZ limited to a small patch in the south-western part of the study area. This area coincides with the deepest part of Isfjorden, where thermobaric stability appears to be less sensitive to thermal variability and dominated by the pressure component. While several pockmarks are still in proximity (but no longer within) the GHSZ, none of the flares are. Coupled with the p90-T thermal regime (F), the modelled lateral extent covered less than 1% of the fjord area, a factor 36 areal decrease compared to A and a factor 9 compared to scenario C.

Isfjorden cross-section. The impact of thermal conditions on GHSZ thickness is illustrated in Fig. 7 through implementation of the p10-T (A) and p90-T (B) thermal models along a key geotransect (Blinova et al., 2012). While zones of NGH-stability are predicted for 95:5 Me:Et gas compositions, no such zones are predicted for pure methane compositions. The GHSZ is shown to retreat and disperse when defined by the less-favourable p90-T thermal conditions. Locally, zones of upper phase boundary deflection are transected, which are identified as local GHSZ patches starting at depths below the seafloor.

The transect passes through the CSB and covers outcropping units of Quaternary-Carboniferous age, with older strata observed towards the east. Several faults reach the seafloor over the length of the cross-section, including the large regional BFZ. Pockmarks and flares are found within 250 m of the transect and generally near surfacing faults and/or sub-cropping thrusts. Along with organic-rich mudstones, these fluid conduits are found within or near the predicted hydrate-stable regime. There is no clear indication of bottom-simulating reflectors (BSRs) in seismic lines ST8815-222 and ST8515-121 (Fig. 7).

Temporal cross-sections in Isfjorden. GHSZ variability results from seasonal-decadal changes in water column and bottom-water temperatures are shown in Fig. 8 along the established Isfjorden transect (Skogseth et al., 2020). Each of the four historical mean water column and bottom-water temperature trends (A–D) show a general temperature decrease along the profile from CTD location 1 to 20. Lower temperatures are observed for the winter months (A, C) and higher temperatures for the summer seasons (B, D). The highest fluctuations are found close to the surface and in shallow waters. Comparison between winters and summers also illustrates the barrier effect. Even in summer, cold and dense water remains trapped and shielded from the inflow of warm water from the shelf behind the igneous sill found near CTD cluster location 14.

Pure methane hydrate stability is only observed for the 2000–2009 winter p50-T thermal regimes. Winter-on-winter comparison shows a decrease of 50%, and the lower phase boundary retreated from a maximum depth of 310 m to 230 m for a 95:5 Me:Et gas composition. A

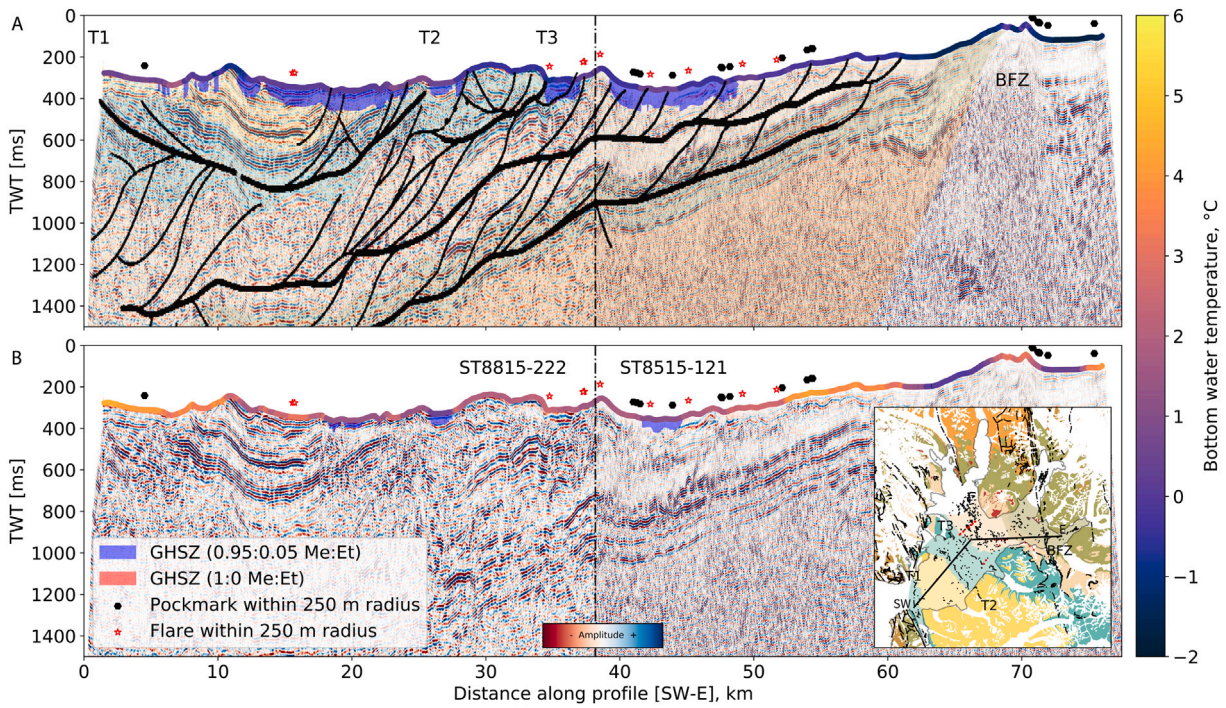

Fig. 7. Key geological cross-section from seismic interpretation by Blinova et al. (2012) overlain with GHSZ extents for the p10-T (A) and p90-T (B) BWT conditions. Pockmarks and flares within 250 m from the transect are projected along the seafloor. Some of the pockmarks are within 5–10 m of the seismic section and have been closely associated with sub-cropping thrusts (Roy et al., 2019, 2016, 2015, 2014). Faults and stratigraphic interpretations are not shown in the bottom profile to illustrate the seismic image clearly. The location of the seismic transect across Isfjorden is shown in the inset geological map (Blinova et al., 2012). Pockmarks and flares within 250 m of the transect have been projected onto the profile. BFZ: Billefjorden Fault Zone.

smaller retreat (225 m to 210 m) was found for the summer-on-summer comparison (−25%), which was in line with seasonal-decadal thermal variations. While mostly governed by the upward migration of the base of the stability zone, vertical thinning also resulted from a significant retreat of the upper boundary. Fig. 6E and F show this and the overall GHSZ retreat when the current value of decadal warming (0.7 and 0.6 °C per decade for winter and summer, respectively) was applied to the 2010–2019 interval. Further fragmentation coincided with vertical thinning and retreat of the upper boundary, as evident from the GHSZ extent between CTD cluster locations 17 and 20. In comparison with A and B, maximum thicknesses for E and F were limited to 155 m and 125 m, respectively, and the corresponding extents for E and F were reduced to just 17% and 24% of those recorded for A and B. Winter extent of the GHSZ along the transect surpassed summer extent by 60 to 130% for each decade, but generally followed a similar but stronger trend of decline.

Several pockmarks and flare locations are found near the maximum extent of GHSZ variability. The dynamic behaviour of the GHSZ illustrates the dynamicity and temperature-relation of vertical GHSZ extent and the zone's downward propagation from the seafloor. An example hereof is found between the CTD cluster locations 18 and 20. Separation of the upper phase boundary and the seafloor gradually leads to the full dissociation of the local GHSZ as the thermal regimes increases from A through F, simultaneously softening the rounded distortion ("bulge"; Fig. 8) of the zone's outer perimeter.

4. Discussion

To correctly assess marine GHSZ potential in its geological context, special attention is first given to the implemented chemothermal conditions and parameter impact assessment. We then put the model outcomes into a geological perspective to narrow down the scope of future exploration efforts in Isfjorden and beyond.

4.1. Model parameter sensitivity analysis

Betlem et al. (2019) provides an extensive sensitivity analysis covering the impact of e.g. geothermal gradients, surface thermal regimes and chemical compositions on GHSZ extent onshore Svalbard. As this contribution implemented few of the same data sources, the discussion that follows only provides a brief overview of the aspects significantly differing from Betlem et al. (2019).

The NN approach provides an alternative to the common approaches of e.g. fixed-extent binning and kriging. The method was designed to better capture the CTD data's full water column data while foregoing a potentially computationally-heavy method (e.g., Wojciech, 2018) applied to thousands of datasets with up to hundreds entries each.

Small changes in bathymetry have been shown to affect thermal water column conditions as Svalbard's fjords are stratified (e.g., Mau et al., 2013; Skogseth et al., 2020). In Svalbard's shallow fjords the bathymetry changes significantly even within small areas, and such changes have a big impact on local conditions. This is for example evident from Adolfbukta in inner Billefjorden, where deeper depths and colder waters are found behind the shallow igneous sill and in proximity to the retreating Nordenskiöld glacier (Rachlewicz et al., 2007; Nilsen et al., 2008; Skogseth et al., 2020). Both the dynamic binning extent and the interpolation of BWTs from available mid-water column data are thus needed to account for local conditions.

When only CTD data within the NN radius are considered, areas with sub-ideal CTD data coverage (e.g., single year, single season; Fig. 2) adversely affected the range and statistical characterisation of water column trends and BWTs. This is locally seen in the non-uniqueness of the BWTs associated with the p50-T base case and the p10-T and p90-T end-member cases (Fig. 4) and likely to have happened regardless of the interpolation method used. For example, areas like eastern Van Keulenfjorden feature unexpectedly high BWTs irrespective of the scenario. With sea ice present well into the summer, such local anomalies likely result from data scarcity and/or seasonal sampling bias. While the local data scarcity and non-uniqueness

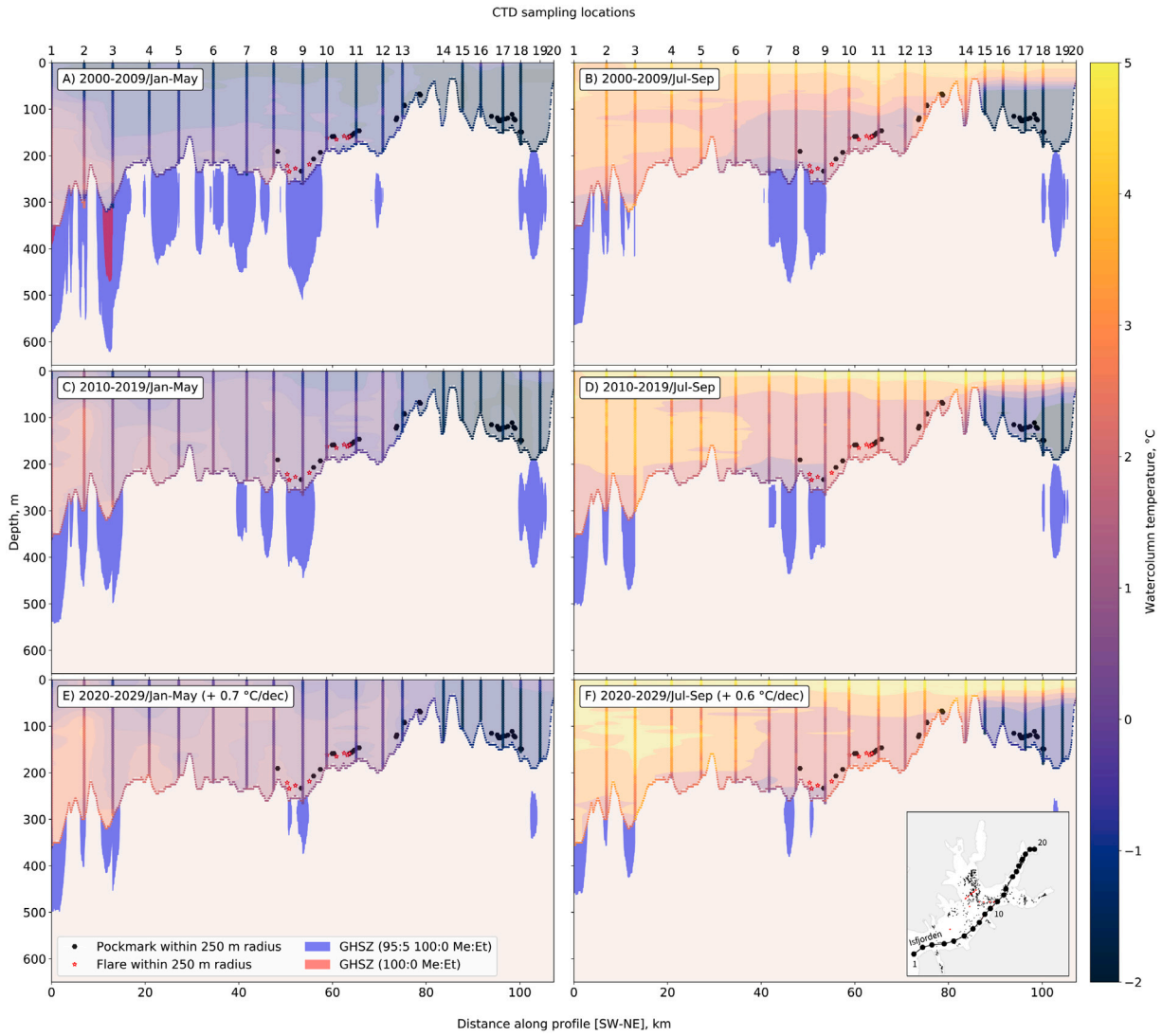

Fig. 8. Temporal GHSZ cross-sections along 20 high-confidence CTD data-cluster sites in Isfjorden. Water column temperature calculations implemented all CTD within a 500 m NN radius within the specified date–time ranges and allowed for a 25 m depth discrepancy between CTD and bathymetry. Inset: location of pockmarks, known flares, and the transect and CTD data-cluster sites in Isfjorden. Pockmarks and flares within 250 m of the transect have been projected onto the profile.

complicates the quantification of the BWT variability and lowers the confidence of the calculated GHSZ in those areas, it does not affect confidence in the archipelago-wide analysis as a whole. The archipelago-wide analysis of p10 and p90 BWT end-member cases provide useful constraints.

The 10th and 90th percentile end-members were primarily taken based on the distribution of water column temperature data within Svalbard's fjords. More specifically, the chosen end-members best resembled the coldest and warmest of the multitude of seasonal types and associated temperature trends observed in Isfjorden (Skogseth et al., 2020). Indeed, this captures the skewed distribution of water column temperature as a result of sea ice formation (lower limit of −1.9 °C). The chosen end-members are thus linked to known phenomena and provide qualitative insights into how they may affect the GHSZ.

Only limited variability in salinity was observed for Svalbard's fjords. Salinity concentrations were mostly limited to the uppermost 40–50 m of the water column and deviated by no more than a few ppt from the 35 ppt salinity assumption. The impact of such deviations on the phase boundary curves is negligible compared to other uncertainties. As such, it did not warrant the inclusion of geospatial salinity calculations through the NN method.

4.2. A hybrid setting - the impact of lateral and temporal temperature change

Parts of Svalbard's fjords feature cold (T < −1.5 °C) and dense water even in summer (e.g., Skogseth et al., 2020). Analogous to the Laptev Sea, where subsea permafrost is widespread (e.g., Delisle, 2000), discontinuous, shallow subsea permafrost may be present in Svalbard's shallow fjords. Indeed, it is perhaps not surprising that the modelled GHSZ feature aspects more commonly associated with the permafrost-affected hydrate setting (Ruppel, 2011; Ruppel and Kessler, 2017), including the behaviour in which NGH are not necessarily stable at the seafloor or surface. As seen in Fig. 8, hydrate-stable conditions are locally only met at a certain depth below the seafloor. Small changes in bathymetry are seemingly enough to tip the thermobaric conditions in or out of the hydrate stable regime at the seafloor (Fig. 9). This results in a "bulge" where the seafloor shoals upwards, with the thermobaric conditions in the subsurface increasingly beyond the hydrate stable regime (Fig. 9, a transition from 4 to 3). Ultimately, the thermobaric regimes become hydrate unstable altogether (e.g., 2 to 1). This phenomenon has previously been associated with shallow marine waters in low geothermal gradient settings (Gorman and Senger, 2010) and in deeper marine environments at high latitudes (Ruppel, 2011).

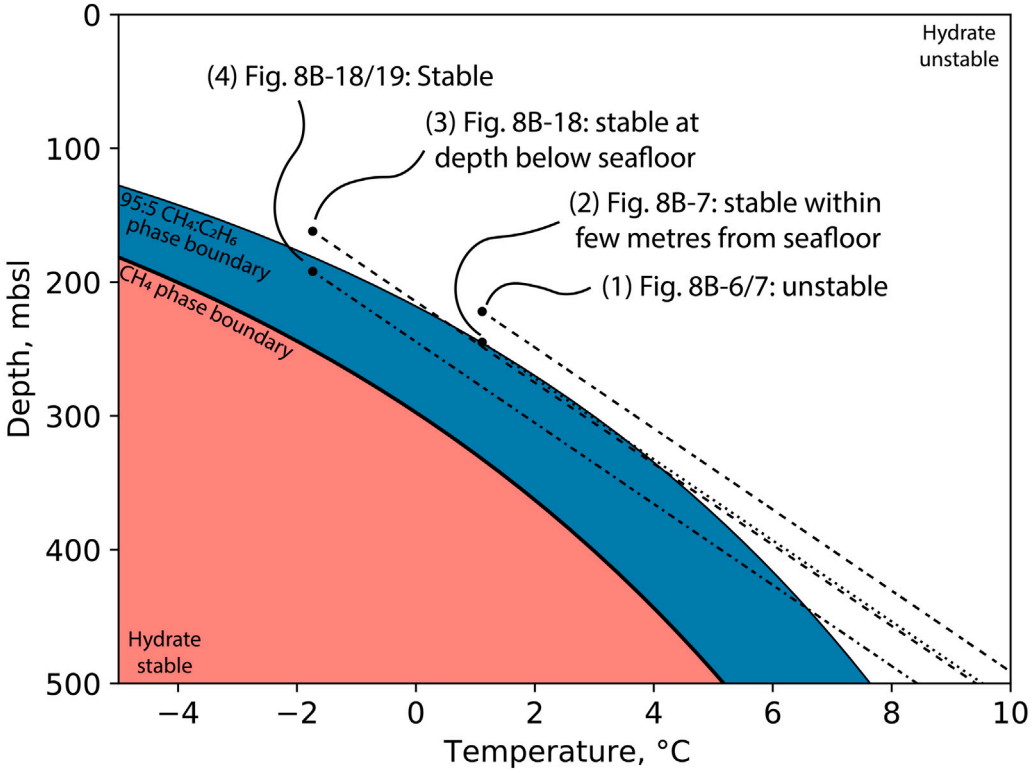

Fig. 9. Schematic of possible GHSZ conditions within Svalbard's fjords for a pure methane and 95:5 Me:Et gas feed. Conditions include NGH *unstable* (1), *stable at depth* (2,3), and *stable at seafloor* (4) thermobaric conditions. The seafloor thermobaric conditions are indicated by a dot for each situation, with the dashed lines indicating subsurface thermobaric conditions (hydrostatic pressure, 33 °C/km geothermal gradient). Each condition contains a reference to a representative location along the transect depicted in Fig. 8. This is either the CTD data station ("18") or a location between two CTD data stations ("6/7").

Such behaviour is further common for the onshore setting (e.g., Betlem et al., 2019; Ruppel and Kessler, 2017), where the GHSZ rarely extends downwards from the surface.

The hybrid setting predicted for the majority of Svalbard's fjords appears to fluctuate around a tipping point of bottom-water NGH stability, a state not unlike that predicted for onshore Svalbard (Betlem et al., 2019). This is a fragile balance likely affected by the observed increase in water column temperatures in Svalbard's fjords. In and around Svalbard, seasonal depths of zero amplitude vary between 5 and 10 m, with higher seasonal seafloor temperature differences giving rise to deeper penetrations. Where present within this interval, seasonal warming has the potential to destabilise the shallowest part of the GHSZ (Wallmann et al., 2018; Riedel et al., 2018).

Decadal trends generally have a deeper penetration into the subsurface than seasonal temperature fluctuations. Reflecting this, the archipelago-wide modelling results indicate an ongoing destabilisation of the GHSZ in Svalbard's fjords. This trend likely becomes increasingly permanent in a warming Arctic as future winter conditions approach the warmest of current summer conditions (Fig. 8E and F). Based on median climate response scenarios, temperatures in the Arctic are predicted to increase by as much as 13 °C (Overland et al., 2014). The surface heat is likely to propagate through the water column and into the sediments. Already at a tipping point of hydrate stability, decadal warming of the water column is likely to cause the GHSZ to thin and retreat to deeper waters before disappearing altogether. Based on the modelling outcomes, destabilisation of Svalbard's near-shore GHSZ potential is possible within the next two to three decades.

4.3. Potential hotspots in Isfjorden and beyond: source rocks and fluid seeps

The absence of BSRs does not rule out NGH and may be explained through many possible reasons (Majumdar et al., 2016). Hard fjord bottom, high velocity sediments and poor-quality 2D seismic data make the identification of BSRs especially difficult. No bottom simulating reflectors (BSRs) have been identified in Svalbard so far. This complicates targeted surveying that is needed to validate our models. The predicted GHSZ extents thus function primarily as constraints for future exploration: combined with geological knowledge and water column data, the models provide best-estimates on where to look next.

Major NS trending fault systems, thrust faults associated with Palaeogene transpression (Blinova et al., 2012; Roy et al., 2019) and igneous intrusions (Senger et al., 2013) provide potential fluid migration pathways. High resolution acoustic shallow sub-bottom data, shale-gas containing formations outcropping at the seafloor, methane supersaturation, and the documented occurrence of flares in the water column support widespread gas migration. NGH stability is predicted for many of these areas. Enhanced acoustic reflections indicative of shallow gas accumulations have been observed within the penetration depth of seasonal temperature fluctuation (Roy et al., 2014, 2019). Where present, NGH may give rise to the phenomenon of seasonal gas migration that has previously been observed offshore Svalbard (e.g., Ferré et al., 2020; Portnov et al., 2016). Indeed, seasonally-unstable NGH may contribute to the pronounced seasonal and spatial variations in the methane excess levels in Isfjorden (Damm et al., 2021). Future exploration should focus on the pressure coring of sediment-core samples and the occurrence of gas seepage within the modelled GHSZ extent, not least addressing the potential occurrence of temporal NGH destabilisation within Svalbard's fjords.

Svalbard's geological record comprises organic-rich source rocks at a number of stratigraphic intervals. In central Spitsbergen, some of these, particularly the organic-rich sequences that make up the Agardhfjellet Formation and Botneheia Formation, may act as unconventional reservoirs hosting shale gas (Fig. 1). Where these are present within the GHSZ, it is possible to envision naturally occurring disseminated NGHs within these zones. Elsewhere, methane-dominated and even biogenic NGH may occur at greater depth where thermobaric conditions remain hydrate-favourable throughout the year.

5. Conclusion

In this study we calculated the gas hydrate stability zone (GHSZ) for Svalbard's fjords based on statistically determined bottom-water temperature (BWT) trends. We implemented gas feeds consisting of pure methane (e.g., biogenic origins) and gas comprising 95% methane and 5% ethane. The assessment of the generated GHSZ models led to the following conclusions regarding the natural gas hydrate (NGH) formation potential in Svalbard's fjords:

- Hydrate stability varies significantly between the 50th percentile BWT base case scenario and the statistically determined 10th and 90th percentile BWT end-members.
- Pure methane gas hydrate-stable conditions are only met in the deepest parts of Isfjorden, Hinlopenstretet, Kross- and Kongsfjorden, and Rijpfjorden.
- The GHSZ is more extensive and thicker for gas compositions with higher percentages of higher-order hydrocarbons.
- Proven source rocks and an active petroleum system increase the likelihood of thermogenic NGH occurrence in Svalbard's fjords. The possibility of hydrate formation with higher-order hydrocarbons is further strengthened by the presence of shallow gas and active gas seepage within the fjords as evidenced by seepage features, some of which newly identified in this study.
- Decadal temperature change negatively impacts GHSZ extent, possibly resulting in a complete disappearance of the GHSZ in Svalbard's fjords if current warming trends continue.

In summary, the majority of Svalbard's fjords feature suitable thermobaric conditions, an active petroleum system, and ongoing fluid seepage that fulfil the main hydrate formation criteria. The assessment conducted in this study is the first step to establish near-shore Svalbard as a potential NGH province. Where shale gas-bearing formations are present within the GHSZ, it is easy to envision naturally occurring disseminated gas hydrate within these zones. This is possibly the case for the flares identified in Isfjorden, which are the current best candidates for where to look next for naturally occurring gas hydrates in Svalbard.

CRediT authorship contribution statement

Peter Betlem: Conceptualization, Methodology, Software, Validation, Formal analysis, Investigation, Resources, Data curation, Writing - original draft, Writing - review & editing, Visualization, Project administration, Funding acquisition. **Srikumar Roy:** Conceptualization, Data curation, Methodology, Validation, Formal analysis, Investigation, Resources, Writing - review & editing, Supervision. **Thomas Birchall:** Formal analysis, Writing - review & editing. **Andrew Hodson:** Resources, Writing - review & editing, Funding acquisition. **Riko Noormets:** Methodology, Investigation, Resources, Data curation, Writing - review & editing. **Miriam Römer:** Methodology, Formal analysis, Investigation, Resources, Data curation, Writing - reviewing & editing. **Ragnheid Skogseth:** Methodology, Resources, Writing - reviewing & editing. **Kim Senger:** Conceptualization, Resources, Writing - review & editing, Supervision, Funding acquisition.

Declaration of competing interest

The authors declare that they have no known competing financial interests or personal relationships that could have appeared to influence the work reported in this paper.

Acknowledgments

This study was partly funded by the Norwegian CCS Research Centre (NCCS; industry partners and The Research Council of Norway (RCN) grant number 257579), CLIMAGAS (RCN grant number 294764), and the Research Centre for Arctic Petroleum Exploration (ARCEx; industry partners and RCN grant number 228107), in addition to funding received by PB from the Petroleum Research School of Norway. SR thanks the Irish Research Council Government of Ireland for the Postdoctoral Fellow Award (Project No. GOIPD/2018/17) and research grant from Science Foundation Ireland (SFI) under grant number 13/RC/2092, co-funded under the European Regional Development Fund and by iCRAG industry partners.

We sincerely appreciate the data provided by the UNIS CO_2 lab (http://CO2-ccs.unis.no/), and particularly the gas data sampled and analysed by IFE. MR thanks the crew and chief scientist Dr. Susan Mau during R/V Heincke cruise HE449 for their support to enable and conduct hydroacoustic water column mapping. Norsk Polar Navigasjon and the Norwegian Petroleum Directorate provided petroleum exploration well data and the Norwegian Polar Institute provided digital topographic and geological maps. Schlumberger and Cegal provided academic licences of Petrel and the Blueback Toolbox, respectively. We sincerely appreciate technical discussions with many of our colleagues, in particular, Ewa Burwicz, Gareth Lord and Snorre Olaussen, and everyone else that provided technical input. Finally, we thank three anonymous reviewers and Editorial Supervisor Zhien Zhang for their constructive input.

Data availability

Datasets related to this article can be found online at https://doi.org/10.5281/zenodo.5091765, hosted at Zenodo (Betlem, 2021).

Appendix A. Supplementary data

Supplementary material related to this article can be found online at https://doi.org/10.1016/j.jngse.2021.104127.

References

Abay, T.B., Karlsen, D.A., Lerch, B., Olaussen, S., Pedersen, J.H., Backer-Owe, K., 2017. Migrated petroleum in outcropping mesozoic sedimentary rocks in Spitsbergen: Organic geochemical characterization and implications for regional exploration. J. Petrol. Geol. 40 (1), 5–36. http://dx.doi.org/10.1111/jpg.12662.

Abay, T.B., Karlsen, D.A., Pedersen, J.H., 2014. Source rocks at Svalbard: An overview of Jurassic and Triassic formations and comparison with offshore Barents Sea time equivalent source rock formations. AAPG Datapages Search and Discovery Article 30372.

Amundsen, H.E.F., Griffin, W.L., O'reilly, S.Y., 1988. The nature of the lithosphere beneath northwestern Spitsbergen: Xenolith evidence. In: Progress in Studies of the Lithosphere in Norway, Norges Geologiske Undersøkelse Special Publication 3, 58–65.

von Appen, W.-J., Schauer, U., Hattermann, T., Beszczynska-Möller, A., 2016. Seasonal cycle of mesoscale instability of the west spitsbergen current. J. Phys. Oceanogr. 46 (4), 1231–1254. http://dx.doi.org/10.1175/JPO-D-15-0184.1.

Avlonitis, D., Danesh, A., Todd, A.C., 1994. Prediction of VL and VLL equilibria of mixtures containing petroleum reservoir fluids and methanol with a cubic EoS. Fluid Phase Equilib. 94, 181–216. http://dx.doi.org/10.1016/0378-3812(94)87057-8.

Bælum, K., Braathen, A., 2012. Along-strike changes in fault array and rift basin geometry of the carboniferous billefjorden trough, Svalbard, Norway. Tectonophysics 546–547, 38–55. http://dx.doi.org/10.1016/j.tecto.2012.04.009.

Bælum, K., Johansen, T.A., Johnsen, H., Rød, K., Ole Ruud, B., Braathen, A., 2012. Subsurface structures of the longyearbyen CO2 lab study area in Central Spitsbergen (Arctic Norway), as mapped by reflection seismic data. Nor. J. Geol. 92 (4).

Baeten, N.J., Forwick, M., Vogt, C., Vorren, T.O., 2010. Late Weichselian and Holocene sedimentary environments and glacial activity in Billefjorden, Svalbard. Geol. Soc. Lond. Special Publ. 344 (1), 207–223. http://dx.doi.org/10.1144/SP344.15.

Banks, D., Sletten, R.S., Haldorsen, S., Dale, B., Heim, M., Swensen, B., 1998. The thermal springs of bockfjord, svalbard: Occurrence and major ion hydrochemistry. Geothermics 27 (4), 445–467. http://dx.doi.org/10.1016/S0375-6505(98)00022-4.

Berndt, C., Feseker, T., Treude, T., Krastel, S., Liebetrau, V., Niemann, H., Bertics, V.J., Dumke, I., Dünnbier, K., Ferré, B., Graves, C., Gross, F., Hissmann, K., Hühnerbach, V., Krause, S., Lieser, K., Schauer, J., Steinle, L., 2014. Temporal constraints on hydrate-controlled methane seepage off Svalbard. Science 343 (6168), 284–287. http://dx.doi.org/10.1126/science.1246298.

Betlem, P., 2018. Implications for Gas Hydrate Occurrence: 3D Thermobaric Modelling of Central Spitsbergen (Thesis).

Betlem, P., 2021. Modelled gas hydrate stability zone extents for Svalbard's fjord and near-shore settings. Zenodo, http://dx.doi.org/10.5281/zenodo.5091765.

Betlem, P., Midttømme, K., Jochmann, M., Senger, K., Olaussen, S., 2018. Geothermal gradients on Svalbard, Arctic Norway. In: First EAGE/IGA/DGMK Joint Workshop on Deep Geothermal Energy. European Association of Geoscientists & Engineers, pp. cp–577.

Betlem, P., Senger, K., Hodson, A., 2019. 3D thermobaric modelling of the gas hydrate stability zone onshore central Spitsbergen, Arctic Norway. Mar. Pet. Geol. 100, 246–262. http://dx.doi.org/10.1016/j.marpetgeo.2018.10.050.

Birchall, T., Senger, K., Hornum, M., Olaussen, S., Braathen, A., 2020. Underpressure of the Barents shelf: Causes and implications for hydrocarbon exploration. AAPG Bull. http://dx.doi.org/10.1306/02272019146.

Bjorøy, M., Hall, P.B., Ferriday, I.L., Mørk, A., 2010. Triassic source rocks of the Barents sea and Svalbard. Search Discov. Article 10219, 1–6.

Blinova, M., Faleide, J.I., Gabrielsen, R.H., Mjelde, R., 2012. Seafloor expression and shallow structure of a fold-and-thrust system, Isfjorden, west Spitsbergen. Polar Res. 31 (1), 11209. http://dx.doi.org/10.3402/polar.v31i0.11209.

Blumenberg, M., Weniger, P., Kus, J., Scheeder, G., Piepjohn, K., Zindler, M., Reinhardt, L., 2018. Geochemistry of a middle Devonian cannel coal (Munindalen) in comparison with Carboniferous coals from Svalbard. Arktos 4 (1), 4. http://dx.doi.org/10.1007/s41063-018-0038-y.

Bohrmann, G., 2015. R/V HEINCKE Cruise Report HE450.

Boswell, R., Collett, T.S., 2011. Current perspectives on gas hydrate resources. Energy Environ. Sci. 4 (4), 1206–1215. http://dx.doi.org/10.1039/C0EE00203H.

Braathen, A., Bælum, K., Christiansen, H.H., Dahl, T., Eiken, O., Elvebakk, H., Hansen, F., Hanssen, T.H., Jochmann, M., Johansen, T.A., 2012. The longyearbyen CO2 lab of Svalbard, Norway—initial assessment of the geological conditions for CO2 sequestration. Nor. J. Geol. 92 (4).

Butschek, F., Arosio, R., Austin, W.E.N., Noormets, R., Howe, J.A., 2019. Late Weichselian glacial history of Forlandsundet, western Svalbard: An inter-ice-stream setting. Arktos 5 (1), 1–14. http://dx.doi.org/10.1007/s41063-018-0063-x.

Cottier, F.R., Nilsen, F., Inall, M.E., Gerland, S., Tverberg, V., Svendsen, H., 2007. Wintertime warming of an Arctic shelf in response to large-scale atmospheric circulation. Geophys. Res. Lett. 34 (10), http://dx.doi.org/10.1029/2007GL029948.

Cottier, F.R., Nilsen, F., Skogseth, R., Tverberg, V., Skarðhamar, J., Svendsen, H., 2010. Arctic fjords: A review of the oceanographic environment and dominant physical processes. Geol. Soc. Lond. Spec. Publ. 344 (1), 35–50. http://dx.doi.org/10.1144/SP344.4.

Ćwiąkała, J., Moskalik, M., Forwick, M., Wojtysiak, K., Giżejewski, J., Szczuciński, W., 2018. Submarine geomorphology at the front of the retreating hansbreen tidewater glacier, Hornsund fjord, southwest Spitsbergen. J. Maps 14 (2), 123–134. http://dx.doi.org/10.1080/17445647.2018.1441757.

Dallmann, W.K., Elvevold, S., Gerland, S., Hormes, A., Majka, J., Ottemöller, L., Pavlova, O., Sander, G., 2015. Geoscience Atlas of Svalbard. Norsk Polar Institutt.

Damm, E., Ericson, Y., Falck, E., 2021. Waterside convection and stratification control methane spreading in supersaturated Arctic fjords (Spitsbergen). Cont. Shelf Res. http://dx.doi.org/10.1016/j.csr.2021.104473.

Damm, E., Mackensen, A., Budéus, G., Faber, E., Hanfland, C., 2005. Pathways of methane in seawater: Plume spreading in an Arctic shelf environment (SW-Spitsbergen). Cont. Shelf Res. 25 (12), 1453–1472. http://dx.doi.org/10.1016/j.csr.2005.03.003.

Delisle, G., 2000. Temporal variability of subsea permafrost and gas hydrate occurrences as function of climate change in the Laptev Sea, Siberia. Polarforschung 68, 221–225.

Eiken, O., 1985. Seismic mapping of the post-Caledonian Svalbard. Polar Res. 3 (2), 167–176. http://dx.doi.org/10.3402/polar.v3i2.6950.

Elvebakk, H., 2010. Results of Borehole Logging in Well LYB CO2, Dh4 of 2009, Longyearbyen, Svalbard, Vol. 35. NGU, Trondheim, Norway.

Elverhoi, A., Gronlie, G., 1981. Diagenetic and sedimentologic explanation for high seismic velocity and low porosity in mesozoic-tertiary sediments, Svalbard region. AAPG Bull. 65 (1), 145–153. http://dx.doi.org/10.1306/2F91978D-16CE-11D7-8645000102C1865D.

Ferré, B., Jansson, P.G., Moser, M., Serov, P., Portnov, A., Graves, C.A., Panieri, G., Gründger, F., Berndt, C., Lehmann, M.F., Niemann, H., 2020. Reduced methane seepage from Arctic sediments during cold bottom-water conditions. Nat. Geosci. 13 (2), 144–148. http://dx.doi.org/10.1038/s41561-019-0515-3.

Ferré, B., Mienert, J., Feseker, T., 2012. Ocean temperature variability for the past 60 years on the Norwegian-Svalbard margin influences gas hydrate stability on human time scales. J. Geophys. Res. Oceans 117 (C10), http://dx.doi.org/10.1029/2012JC008300.

Fetterer, F., Knowles, K., Meier, W., Savoie, R., 2016. Sea Ice Index, Version 2. NSIDC, http://dx.doi.org/10.7265/N5736NV7.

Forwick, M., Baeten, N.J., Vorren, T.O., 2009. Pockmarks in Spitsbergen fjords. Nor. J. Geol. 89, 65–77.

Fraser, N.J., Skogseth, R., Nilsen, F., Inall, M.E., 2018. Circulation and exchange in a broad Arctic fjord using glider-based observations. Polar Res. 37 (1), 1485417. http://dx.doi.org/10.1080/17518369.2018.1485417.

Giustiniani, M., Tinivella, U., Jakobsson, M., Rebesco, M., 2014. Arctic ocean gas hydrate stability in a changing climate. J. Geol. Res 2013, http://dx.doi.org/10.1155/2013/783969.

Gorman, A.R., Senger, K., 2010. Defining the updip extent of the gas hydrate stability zone on continental margins with low geothermal gradients. J. Geophys. Res.: Solid Earth 115 (B7), http://dx.doi.org/10.1029/2009JB006680.

Hanssen-Bauer, I., Førland, E., Hisdal, H., Mayer, S., Sandø, A., Sorteberg, A., 2019. Climate in Svalbard 2100–a knowledge base for climate adaptation. Nor. Cent. Clim. Serv.

Harland, W.B., Cutbill, J., Friend, P.F., Gobbett, D.J., Holliday, D., Maton, P., Parker, J., Wallis, R.H., 1974. The Billefjorden Fault Zone, Spitsbergen: The long history of a major tectonic lineament.

Harland, W.B., Pickton, C.A.G., Wright, N.J.R., Croxton, C.A., Smith, D.G., Cutbill, J.L., Henderson, W.G., 1976. Some coal-bearing strata in Svalbard.

Henriksen, E., Bjørnseth, H.M., Hals, T.K., Heide, T., Kiryukhina, T., Kløvjan, O.S., Larssen, G.B., Ryseth, A.E., Rønning, K., Sollid, K., Stoupakova, A., 2011a. Chapter 17 uplift and erosion of the greater Barents Sea: Impact on prospectivity and petroleum systems. Geol. Soc. Lond. Mem. 35 (1), 271–281. http://dx.doi.org/10.1144/M35.17.

Henriksen, E., Ryseth, A.E., Larssen, G.B., Heide, T., Rønning, K., Sollid, K., Stoupakova, A.V., 2011b. Chapter 10 tectonostratigraphy of the greater Barents Sea: Implications for petroleum systems. Geol. Soc. Lond. Mem. 35 (1), 163–195. http://dx.doi.org/10.1144/M35.10.

Himmler, T., Sahy, D., Martma, T., Bohrmann, G., Plaza-Faverola, A., Bünz, S., Condon, D.J., Knies, J., Lepland, A., 2019. A 160,000-year-old history of tectonically controlled methane seepage in the Arctic. Sci. Adv. 5 (8), eaaw1450. http://dx.doi.org/10.1126/sciadv.aaw1450.

Hodson, A.J., Nowak, A., Redeker, K.R., Holmlund, E.S., Christiansen, H.H., Turchyn, A.V., 2019. Seasonal dynamics of methane and carbon dioxide evasion from an open system pingo: Lagoon Pingo, Svalbard. Front. Earth Sci. 7, 30. http://dx.doi.org/10.3389/feart.2019.00030.

Hoel, A., Holtedahl, O., 1911. Les nappes de lave, les volcans et les sources thermales dans les environs de La Baie Wood. Videnskapsselsk. Skr. M.-N. Kl. Kristiania (8).

House, K.Z., Schrag, D.P., Harvey, C.F., Lackner, K.S., 2006. Permanent carbon dioxide storage in deep-sea sediments. Proc. Natl. Acad. Sci. 103 (33), 12291–12295. http://dx.doi.org/10.1073/pnas.0605318103.

Høyland, K.V., 2009. Ice thickness, growth and salinity in Van Mijenfjorden, Svalbard, Norway. Polar Res. 28 (3), 339–352. http://dx.doi.org/10.1111/j.1751-8369.2009.00133.x.

Huq, F., Smalley, P.C., Mørkved, P.T., Johansen, I., Yarushina, V., Johansen, H., 2017. The longyearbyen CO2 lab: Fluid communication in reservoir and caprock. Int. J. Greenh. Gas Control 63, 59–76. http://dx.doi.org/10.1016/j.ijggc.2017.05.005.

IPCC, 2014. AR5 Climate Change 2014: Mitigation of Climate Change. Technical Report.

Isaksen, K., Nordli, Ø., Førland, E.J., Łupikasza, E., Eastwood, S., Niedźwiedź, T., 2016. Recent warming on Spitsbergen—influence of atmospheric circulation and sea ice cover. J. Geophys. Res.: Atmos. 121 (20), 11,913–11,931. http://dx.doi.org/10.1002/2016JD025606.

Jakobsson, M., Mayer, L.A., Bringensparr, C., Castro, C.F., Mohammad, R., Johnson, P., Ketter, T., Accettella, D., Amblas, D., An, L., Arndt, J.E., Canals, M., Casamor, J.L., Chauché, N., Coakley, B., Danielson, S., Demarte, M., Dickson, M.-L., Dorschel, B., Dowdeswell, J.A., Dreutter, S., Fremand, A.C., Gallant, D., Hall, J.K., Hehemann, L., Hodnesdal, H., Hong, J., Ivaldi, R., Kane, E., Klaucke, I., Krawczyk, D.W., Kristoffersen, Y., Kuipers, B.R., Millan, R., Masetti, G., Morlighem, M., Noormets, R., Prescott, M.M., Rebesco, M., Rignot, E., Semiletov, I., Tate, A.J., Travaglini, P., Velicogna, I., Weatherall, P., Weinrebe, W., Willis, J.K., Wood, M., Zarayskaya, Y., Zhang, T., Zimmermann, M., Zinglersen, K.B., 2020. The international bathymetric chart of the Arctic Ocean Version 4.0. Sci. Data 7 (1), 176. http://dx.doi.org/10.1038/s41597-020-0520-9.

James, R.H., Bousquet, P., Bussmann, I., Haeckel, M., Kipfer, R., Leifer, I., Niemann, H., Ostrovsky, I., Piskozub, J., Rehder, G., Treude, T., Vielstädte, L., Greinert, J., 2016. Effects of climate change on methane emissions from seafloor sediments in the Arctic Ocean: A review. Limnol. Oceanogr. 61 (S1), S283–S299. http://dx.doi.org/10.1002/lno.10307.

Johnson, A.H., 2011. Global resource potential of gas hydrate–a new calculation. Fire in the Ice 11 (2), 1–3.

Kempf, P., Forwick, M., Laberg, J.S., Vorren, T.O., 2013. Late Weichselian and Holocene sedimentary palaeoenvironment and glacial activity in the high-arctic van Keulenfjorden, Spitsbergen. Holocene 23 (11), 1607–1618. http://dx.doi.org/10.1177/0959683613499055.

Kihara, T., 1953. Virial coefficients and models of molecules in gases. Rev. Modern Phys. 25 (4), 831–843. http://dx.doi.org/10.1103/RevModPhys.25.831.

Knies, J., Damm, E., Gutt, J., Mann, U., Pinturier, L., 2004. Near-surface hydrocarbon anomalies in shelf sediments off Spitsbergen: Evidences for past seepages. Geochem. Geophys. Geosyst. 5 (6), http://dx.doi.org/10.1029/2003GC000687.

Knies, J., Plaza-Faverola, A., Bünz, S., Mienert, J., Daszinnies, M., Mattingsdal, R., Chand, S., 2015. Finding the source for hydrocarbon leakage on the Vestnesa Ridge, NW Svalbard. In: OTC Arctic Technology Conference. Offshore Technology Conference, http://dx.doi.org/10.4043/25483-MS.

Koevoets, M.J., Abay, T.B., Hammer, Ø., Olaussen, S., 2016. High-resolution organic carbon–isotope stratigraphy of the middle Jurassic–lower cretaceous Agardhfjellet formation of central Spitsbergen, Svalbard. Palaeogeogr. Palaeoclimatol. Palaeoecol. 449, 266–274. http://dx.doi.org/10.1016/j.palaeo.2016.02.029.

Kvenvolden, K.A., 1998. A primer on the geological occurrence of gas hydrate. Geol. Soc. Lond. Spec. Publ. 137 (1), 9–30. http://dx.doi.org/10.1144/GSL.SP.1998.137.01.02.

Kvenvolden, K.A., Lorenson, T.D., 2001. The global occurrence of natural gas hydrate. In: Natural Gas Hydrates: Occurrence, Distribution, and Detection. American Geophysical Union (AGU), pp. 3–18. http://dx.doi.org/10.1029/GM124p0003.

Lasabuda, A., Laberg, J.S., Knutsen, S.-M., Safronova, P., 2018. Cenozoic tectonostratigraphy and pre-glacial erosion: A mass-balance study of the Northwestern Barents Sea margin, Norwegian Arctic. J. Geodyn. 119, 149–166. http://dx.doi.org/10.1016/j.jog.2018.03.004.

Liira, M., Noormets, R., Sepp, H., Kekišev, O., Maddison, M., Olaussen, S., 2019. Sediment geochemical study of hydrocarbon seeps in Isfjorden and Mohnbukta: A comparison between Western and Eastern Spitsbergen, Svalbard. Arktos 5 (1), 49–62. http://dx.doi.org/10.1007/s41063-019-00067-7.

Lowell, J.D., 1972. Spitsbergen tertiary orogenic belt and the Spitsbergen fracture zone. GSA Bull. 83 (10), 3091–3102. http://dx.doi.org/10.1130/0016-7606(1972)83[3091:STOBAT]2.0.CO;2.

Luckman, A., Benn, D.I., Cottier, F., Bevan, S., Nilsen, F., Inall, M., 2015. Calving rates at tidewater glaciers vary strongly with ocean temperature. Nature Commun. 6 (1), 8566. http://dx.doi.org/10.1038/ncomms9566.

Maciejowski, W., Michniewski, A., 2007. Variations in weather on the east and west coasts of South Spitsbergen, Svarbald. Polish Polar Res. 28 (2).

Majumdar, U., Cook, A.E., Shedd, W., Frye, M., 2016. The connection between natural gas hydrate and bottom-simulating reflectors. Geophys. Res. Lett. 43 (13), 7044–7051. http://dx.doi.org/10.1002/2016GL069443.

Marín-Moreno, H., Minshull, T.A., Westbrook, G.K., Sinha, B., Sarkar, S., 2013. The response of methane hydrate beneath the seabed offshore Svalbard to ocean warming during the next three centuries. Geophys. Res. Lett. 40 (19), 5159–5163. http://dx.doi.org/10.1002/grl.50985.

Masoudi, R., Tohidi, B., Danesh, A., Todd, A.C., 2004. A new approach in modelling phase equilibria and gas solubility in electrolyte solutions and its applications to gas hydrates. Fluid Phase Equilib. 215 (2), 163–174. http://dx.doi.org/10.1016/j.fluid.2003.08.009.

Mau, S., Blees, J., Helmke, E., Niemann, H., Damm, E., 2013. Vertical distribution of methane oxidation and methanotrophic response to elevated methane concentrations in stratified waters of the Arctic fjord storfjorden (Svalbard, Norway). Biogeosciences 10 (10), 6267–6278. http://dx.doi.org/10.5194/bg-10-6267-2013.

Mau, S., Römer, M., Torres, M.E., Bussmann, I., Pape, T., Damm, E., Geprägs, P., Wintersteller, P., Hsu, C.-W., Loher, M., Bohrmann, G., 2017. Widespread methane seepage along the continental margin off Svalbard - from Bjørnøya to Kongsfjorden. Sci. Rep. 7 (1), 42997. http://dx.doi.org/10.1038/srep42997.

Max, M.D., Johnson, A.H., Dillon, W.P., 2005. Economic Geology of Natural Gas Hydrate. Springer Science & Business Media.

McConnell, D.R., Zhang, Z., Boswell, R., 2012. Review of progress in evaluating gas hydrate drilling hazards. Mar. Pet. Geol. 34 (1), 209–223. http://dx.doi.org/10.1016/j.marpetgeo.2012.02.010.

McKinney, W., 2011. Pandas: A foundational python library for data analysis and statistics. Python High Perform. Sci. Comput. 14 (9), 9.

Midttømme, K., Jochmann, M., Henne, I., Wangen, M., Thomas, P.J., 2015. Is geothermal energy an alternative for Svalbard? In: The Third Sustainable Earth Sciences Conference and Exhibition, Vol. 2015. European Association of Geoscientists & Engineers, pp. 1–5. http://dx.doi.org/10.3997/2214-4609.201414251.

Milkov, A.V., 2004. Global estimates of hydrate-bound gas in marine sediments: How much is really out there? Earth-Sci. Rev. 66 (3), 183–197. http://dx.doi.org/10.1016/j.earscirev.2003.11.002.

Minshull, T.A., Marín-Moreno, H., Betlem, P., Bialas, J., Bünz, S., Burwicz, E., Cameselle, A.L., Cifci, G., Giustiniani, M., Hillman, J.I., Hölz, S., Hopper, J.R., Ion, G., León, R., Magalhaes, V., Makovsky, Y., Mata, M.-P., Max, M.D., Nielsen, T., Okay, S., Ostrovsky, I., O'Neill, N., Pinheiro, L.M., Plaza-Faverola, A.A., Rey, D., Roy, S., Schwalenberg, K., Senger, K., Vadakkepuliyambatta, S., Vasilev, A., Vázquez, J.-T., 2020. Hydrate occurrence in Europe: A review of available evidence. Mar. Pet. Geol. 111, 735–764. http://dx.doi.org/10.1016/j.marpetgeo.2019.08.014.

Mjelde, R., 2005. Geoscience education and research at the University of Bergen. First Break 23 (8), http://dx.doi.org/10.3997/1365-2397.23.8.26664.

Mørk, A., Bjorøy, M., 1984. Mesozoic source rocks on Svalbard. In: Spencer, A.M. (Ed.), Petroleum Geology of the North European Margin. Springer Netherlands, Dordrecht, pp. 371–382. http://dx.doi.org/10.1007/978-94-009-5626-1_28.

Muckenhuber, S., Nilsen, F., Korosov, A., Sandven, S., 2016. Sea ice cover in Isfjorden and Hornsund, Svalbard (2000–2014) from remote sensing data. Cryosphere 10 (1), 149–158. http://dx.doi.org/10.5194/tc-10-149-2016.

Nicolaisen, J.B., Elvebakk, G., Ahokas, J., Bojesen-Koefoed, J.A., Olaussen, S., Rinna, J., Skeie, J.E., Stemmerik, L., 2019. Characterization of upper palaeozoic organic-rich units in Svalbard: Implications for the petroleum systems of the Norwegian Barents Shelf. J. Petrol. Geol. 42 (1), 59–78. http://dx.doi.org/10.1111/jpg.12724.

Nilsen, F., Cottier, F., Skogseth, R., Mattsson, S., 2008. Fjord–shelf exchanges controlled by ice and brine production: The interannual variation of Atlantic water in Isfjorden, Svalbard. Cont. Shelf Res. 28 (14), 1838–1853. http://dx.doi.org/10.1016/j.csr.2008.04.015.

Nilsen, F., Skogseth, R., Vaardal-Lunde, J., Inall, M., 2016. A simple shelf circulation model: Intrusion of Atlantic water on the West Spitsbergen Shelf. J. Phys. Oceanogr. 46 (4), 1209–1230. http://dx.doi.org/10.1175/JPO-D-15-0058.1.

Nordli, Ø., Przybylak, R., Ogilvie, A.E.J., Isaksen, K., 2014. Long-term temperature trends and variability on Spitsbergen: The extended Svalbard airport temperature series, 1898–2012. Polar Res. 33 (1), 21349. http://dx.doi.org/10.3402/polar.v33.21349.

Nøttvedt, A., Livbjerg, F., Midbøe, P.S., Rasmussen, E., 1993. Hydrocarbon potential of the Central Spitsbergen Basin. In: Vorren, T.O., Bergsager, E., Dahl-Stamnes, Ø.A., Holter, E., Johansen, B., Lie, E., Lund, T.B. (Eds.), Norwegian Petroleum Society Special Publications, Vol. 2. Elsevier, pp. 333–361. http://dx.doi.org/10.1016/B978-0-444-88943-0.50026-5.

NPI, 2016. Geological map of Svalbard (1:250000). http://dx.doi.org/10.21334/NPOLAR.2016.616F7504.

Ogata, K., Senger, K., Braathen, A., Tveranger, J., Olaussen, S., 2014. Fracture systems and mesoscale structural patterns in the siliciclastic mesozoic reservoir-caprock succession of the longyearbyen CO2 lab project: Implications for geological CO2 sequestration in Central Spitsbergen, Svalbard. Norsk Geologisk Tidsskrift 121–154.

Ohm, S.E., Karlsen, D.A., Austin, T.J.F., 2008. Geochemically driven exploration models in uplifted areas: Examples from the Norwegian Barents Sea. AAPG Bull. 92 (9), 1191–1223. http://dx.doi.org/10.1306/06180808028.

Ohm, S.E., Larsen, L., Olaussen, S., Senger, K., Birchall, T., Demchuk, T., Hodson, A., Johansen, I., Titlestad, G.O., Karlsen, D.A., Braathen, A., 2019. Discovery of shale gas in organic rich Jurassic successions, Adventdalen, Central Spitsbergen, Norway. Nor. J. Geol. 99 (2), http://dx.doi.org/10.17850/njg007.

Olaussen, S., Senger, K., Braathen, A., Grundvåg, S.-A., Mørk, A., 2019. You learn as long as you drill; research synthesis from the longyearbyen CO2 laboratory, Svalbard, Norway. 157-187 http://dx.doi.org/10.17850/njg008.

Onarheim, I.H., Smedsrud, L.H., Ingvaldsen, R.B., Nilsen, F., 2014. Loss of sea ice during winter north of Svalbard. Tellus A 66 (1), 23933. http://dx.doi.org/10.3402/tellusa.v66.23933.

Overland, J.E., Wang, M., Walsh, J.E., Stroeve, J.C., 2014. Future Arctic climate changes: Adaptation and mitigation time scales. Earth's Future 2 (2), 68–74. http://dx.doi.org/10.1002/2013EF000162.

Paech, H.-J., Koch, J., 2001. Coalification in post-Caledonian sediments on Spitsbergen. Geologisches Jahrbuch Reihe B 507–534.

Parrish, W.R., 1972. Dissociation pressures of gas hydrates formed by gas mixtures. Ind. Eng. Chem. Proc. Des. Dev. 11, 26–34.

Pavlov, A.K., Tverberg, V., Ivanov, B.V., Nilsen, F., Falk-Petersen, S., Granskog, M.A., 2013. Warming of atlantic water in two west Spitsbergen fjords over the last century (1912–2009). Polar Res. 32 (1), 11206. http://dx.doi.org/10.3402/polar.v32i0.11206.

Plaza-Faverola, A., Vadakkepuliyambatta, S., Hong, W.-L., Mienert, J., Bünz, S., Chand, S., Greinert, J., 2017. Bottom-simulating reflector dynamics at arctic thermogenic gas provinces: An example from Vestnesa Ridge, offshore west Svalbard. J. Geophys. Res.: Solid Earth 122 (6), 4089–4105. http://dx.doi.org/10.1002/2016JB013761.

Portnov, A., Vadakkepuliyambatta, S., Mienert, J., Hubbard, A., 2016. Ice-sheet-driven methane storage and release in the Arctic. Nature Commun. 7 (1), 1–7. http://dx.doi.org/10.1038/ncomms10314.

Promińska, A., Falck, E., Walczowski, W., 2018. Interannual variability in hydrography and water mass distribution in Hornsund, an Arctic fjord in Svalbard. Polar Res. 37 (1), 1495546. http://dx.doi.org/10.1080/17518369.2018.1495546.

Przybylak, R., Araźny, A., Nordli, Ø., Finkelnburg, R., Kejna, M., Budzik, T., Migała, K., Sikora, S., Puczko, D., Rymer, K., Rachlewicz, G., 2014. Spatial distribution of air temperature on Svalbard during 1 year with campaign measurements. Int. J. Climatol. 34 (14), 3702–3719. http://dx.doi.org/10.1002/joc.3937.

Rachlewicz, G., W, S., M, E., 2007. Post-'Little Ice Age' retreat rates of glaciers around Billefjorden in Central Spitsbergen, Svalbard. Polish Polar Res. 3 (28).

Reigstad, L.J., Jorgensen, S.L., Lauritzen, S.-E., Schleper, C., Urich, T., 2011. Sulfur-oxidizing chemolithotrophic proteobacteria dominate the microbiota in high arctic thermal springs on Svalbard. Astrobiology 11 (7), 665–678. http://dx.doi.org/10.1089/ast.2010.0551.

Riedel, M., Scherwath, M., Römer, M., Veloso, M., Heesemann, M., Spence, G.D., 2018. Distributed natural gas venting offshore along the Cascadia margin. Nature Commun. 9 (1), 1–14. http://dx.doi.org/10.1038/s41467-018-05736-x.

Römer, M., Mau, S., 2015. Swath sonar multibeam bathymetry during HEINCKE cruise HE449 with links to raw data files of bathymetry and water column information, http://dx.doi.org/10.1594/PANGAEA.855885.

Roy, S., Hovland, M., Braathen, A., 2016. Evidence of fluid seepage in Grønfjorden, Spitsbergen: Implications from an integrated acoustic study of seafloor morphology, marine sediments and tectonics. Mar. Geol. 380, 67–78. http://dx.doi.org/10.1016/j.margeo.2016.07.002.

Roy, S., Hovland, M., Noormets, R., Olaussen, S., 2015. Seepage in Isfjorden and its tributary fjords, West Spitsbergen. Mar. Geol. 363, 146–159. http://dx.doi.org/10.1016/j.margeo.2015.02.003.

Roy, S., Senger, K., Braathen, A., Noormets, R., Hovland, M., Olaussen, S., 2014. Fluid migration pathways to seafloor seepage in inner Isfjorden and Adventfjorden, Svalbard. 0029-196X.

Roy, S., Senger, K., Hovland, M., Noormets, R., 2012. Gas hydrate formation potential in the Fjords of Svalbard. In: Arctic Frontiers Conference-Energies of the High North, 22–27 January, Tromsø, Norway, Tromsø.

Roy, S., Senger, K., Hovland, M., Römer, M., Braathen, A., 2019. Geological controls on shallow gas distribution and seafloor seepage in an Arctic fjord of Spitsbergen, Norway. Mar. Pet. Geol. 107, 237–254. http://dx.doi.org/10.1016/j.marpetgeo.2019.05.021.

Ruppel, C.D., 2011. Methane hydrates and contemporary climate change. Nat. Eduction Knowl. 2 (12), 12.

Ruppel, C.D., Kessler, J.D., 2017. The interaction of climate change and methane hydrates: Climate-Hydrates Interactions. Rev. Geophys. 55 (1), 126–168. http://dx.doi.org/10.1002/2016RG000534.

Sahling, H., Römer, M., Pape, T., Bergès, B., dos Santos Fereirra, C., Boelmann, J., Geprägs, P., Tomczyk, M., Nowald, N., Dimmler, W., 2014. Gas emissions at the continental margin west of Svalbard: Mapping, sampling, and quantification. Biogeosciences 11 (21).

Salvigsen, O., Elgersma, A., 1985. Large-scale karst features and open taliks at Vardeborgsletta, outer Isfjorden, Svalbard. Polar Res. 3 (2), 145–153. http://dx.doi.org/10.3402/polar.v3i2.6948.

Senger, K., Brugmans, P., Grundvåg, S.-A., Jochmann, M., Nøttvedt, A., Olaussen, S., Skotte, A., Smyrak-Sikora, A., 2019. Petroleum, coal and research drilling onshore Svalbard: A historical perspective. Nor. J. Geol. 99 (3), http://dx.doi.org/10.17850/njg99-3-1.

Senger, K., Roy, S., Braathen, A., Buckley, S.J., Bælum, K., Gernigon, L., Mjelde, R., Noormets, R., Ogata, K., Olaussen, S., Planke, S., Ruud, B.O., Tveranger, J., 2013. Geometries of doleritic intrusions in central Spitsbergen, Svalbard: An integrated study of an onshore-offshore magmatic province with implications for CO2 sequestration. Norwegian Journal of Geology 93.

Serov, P., Vadakkepuliyambatta, S., Mienert, J., Patton, H., Portnov, A., Silyakova, A., Panieri, G., Carroll, M.L., Carroll, J., Andreassen, K., Hubbard, A., 2017. Postglacial response of Arctic Ocean gas hydrates to climatic amelioration. Proc. Natl. Acad. Sci. 114 (24), 6215–6220. http://dx.doi.org/10.1073/pnas.1619288114.

Shkola, I.V., 1977. Processing Results from Parametric Drill Hole Grumant-1 in Western Svalbard near Coles Bay (Report 5125, Leningrad). All-Russian Research Institute for Geology and Mineral Resources of the World Ocean, St. Petersburg, PANGAEA, http://dx.doi.org/10.1594/PANGAEA.688742.

Skarðhamar, J., Svendsen, H., 2010. Short-term hydrographic variability in a stratified Arctic fjord. Geol. Soc. Lond. Spec. Publ. 344 (1), 51–60. http://dx.doi.org/10.1144/SP344.5.

Skogseth, R., Ellingsen, P., Berge, J., Cottier, F., Falk-Petersen, S., Ivanov, B., Nilsen, F., Søreide, J., Vader, A., 2019. UNIS Hydrographic Database. Norwegian Polar Institute, http://dx.doi.org/10.21334/unis-hydrography.

Skogseth, R., Haugan, P.M., Haarpaintner, J., 2004. Ice and brine production in Storfjorden from four winters of satellite and in situ observations and modeling. J. Geophys. Res. Oceans 109 (C10), http://dx.doi.org/10.1029/2004JC002384.

Skogseth, R., Olivier, L.L.A., Nilsen, F., Falck, E., Fraser, N., Tverberg, V., Ledang, A.B., Vader, A., Jonassen, M.O., Søreide, J., Cottier, F., Berge, J., Ivanov, B.V., Falk-Petersen, S., 2020. Variability and decadal trends in the Isfjorden (Svalbard) ocean climate and circulation - an indicator for climate change in the European Arctic. Prog. Oceanogr. 102394. http://dx.doi.org/10.1016/j.pocean.2020.102394.

Sloan, E.D., Koh, C.A., 2007. Clathrate Hydrates of Natural Gases, Zeroth ed. CRC Press, http://dx.doi.org/10.1201/9781420008494.

Steel, R.J., Dalland, A., Kalgraff, K., Larsen, V., 1981. The central tertiary basin of Spitsbergen: Sedimentary development of a sheared-margin basin. pp. 647–664.

Streuff, K.T., 2013. Landform Assemblages in Inner Kongsfjorden, Svalbard: Evidence of Recent Glacial (Surge) Activity (Ph.D. thesis). Universitetet i Tromsø.

Streuff, K., Ó Cofaigh, C., Noormets, R., Lloyd, J.M., 2017. Submarine landforms and glacimarine sedimentary processes in Lomfjorden, East Spitsbergen. Mar. Geol. 390, 51–71. http://dx.doi.org/10.1016/j.margeo.2017.04.014.

Streuff, K., Ó Cofaigh, C., Noormets, R., Lloyd, J., 2018. Submarine landform assemblages and sedimentary processes in front of Spitsbergen tidewater glaciers. Mar. Geol. 402, 209–227. http://dx.doi.org/10.1016/j.margeo.2017.09.006.

Sultan, N., Cochonat, P., Foucher, J.P., Mienert, J., Haflidason, H., Sejrup, H.P., 2003. Effect of gas hydrates dissociation on seafloor slope stability. In: Locat, J., Mienert, J., Boisvert, L. (Eds.), Submarine Mass Movements and their Consequences: 1st International Symposium. In: Advances in Natural and Technological Hazards Research, Springer Netherlands, Dordrecht, pp. 103–111. http://dx.doi.org/10.1007/978-94-010-0093-2_12.

Tinivella, U., Giustiniani, M., 2016. Gas hydrate stability zone in shallow Arctic Ocean in presence of sub-sea permafrost. Rendiconti Lincei 27 (1), 163–171. http://dx.doi.org/10.1007/s12210-016-0520-z.

Tohidi, B., Danesh, A., Todd, A., 1995. Modeling single and mixed electrolyte-solutions and its applications to gas hydrates. Chem. Eng. Res. Des. 73 (4), 464–472.

Tohidi, B., Yang, J., Salehabadi, M., Anderson, R., Chapoy, A., 2010. CO2 hydrates could provide secondary safety factor in subsurface sequestration of CO2. Environ. Sci. Technol. 44 (4), 1509–1514. http://dx.doi.org/10.1021/es902450j.

Tverberg, V., Skogseth, R., Cottier, F., Sundfjord, A., Walczowski, W., Inall, M.E., Falck, E., Pavlova, O., Nilsen, F., 2019. The Kongsfjorden Transect: Seasonal and inter-annual variability in hydrography. In: Hop, H., Wiencke, C. (Eds.), The Ecosystem of Kongsfjorden, Svalbard. In: Advances in Polar Ecology, Springer International Publishing, Cham, pp. 49–104. http://dx.doi.org/10.1007/978-3-319-46425-1_3.

Vadakkepuliyambatta, S., Chand, S., Bünz, S., 2017. The history and future trends of ocean warming-induced gas hydrate dissociation in the SW Barents Sea. Geophys. Res. Lett. 44 (2), 835–844. http://dx.doi.org/10.1002/2016GL071841.

Valderrama, J.O., 1990. A generalized Patel-Teja equation of state for polar and nonpolar fluids and their mixtures. J. Chem. Eng. Jpn. 23 (1), 87–91. http://dx.doi.org/10.1252/jcej.23.87.

Van Der Waals, J.H., 1959. Clathrate solutions. Adv. Chem. Phys. 2, 1–57.

Verba, M.L., 2007. Natural hydrocarbon manifestations in the sedimentary cover of Svalbard. Petrol. Geol. Theor. Appl. Stud. 2, 1–22.

Verba, M., 2013. Sedimentary cover reservoir of Svalbard archipelago. Neftegazovaya Geologiya. Teoriya I Praktika 8 (1), http://dx.doi.org/10.17353/2070-5379/5_2013.

Virtanen, P., Gommers, R., Oliphant, T.E., Haberland, M., Reddy, T., Cournapeau, D., Burovski, E., Peterson, P., Weckesser, W., Bright, J., van der Walt, S.J., Brett, M., Wilson, J., Millman, K.J., Mayorov, N., Nelson, A.R.J., Jones, E., Kern, R., Larson, E., Carey, C.J., Polat, İ., Feng, Y., Moore, E.W., VanderPlas, J., Laxalde, D., Perktold, J., Cimrman, R., Henriksen, I., Quintero, E.A., Harris, C.R., Archibald, A.M., Ribeiro, A.H., Pedregosa, F., van Mulbregt, P., 2020. SciPy 1.0: Fundamental algorithms for scientific computing in Python. Nat. Methods 17 (3), 261–272. http://dx.doi.org/10.1038/s41592-019-0686-2.

Wallmann, K., Riedel, M., Hong, W.L., Patton, H., Hubbard, A., Pape, T., Hsu, C.W., Schmidt, C., Johnson, J.E., Torres, M.E., Andreassen, K., Berndt, C., Bohrmann, G., 2018. Gas hydrate dissociation off Svalbard induced by isostatic rebound rather than global warming. Nature Commun. 9 (1), 1–9. http://dx.doi.org/10.1038/s41467-017-02550-9.

Weniger, P., Blumenberg, M., Berglar, K., Ehrhardt, A., Klitzke, P., Krüger, M., Lutz, R., 2019. Origin of near-surface hydrocarbon gases bound in northern Barents Sea sediments. Mar. Pet. Geol. 102, 455–476. http://dx.doi.org/10.1016/j.marpetgeo.2018.12.036.

Westbrook, G.K., Thatcher, K.E., Rohling, E.J., Piotrowski, A.M., Pälike, H., Osborne, A.H., Nisbet, E.G., Minshull, T.A., Lanoisellé, M., James, R.H., Hühnerbach, V., Green, D., Fisher, R.E., Crocker, A.J., Chabert, A., Bolton, C., Beszczynska-Möller, A., Berndt, C., Aquilina, A., 2009. Escape of methane gas from the seabed along the West Spitsbergen continental margin. Geophys. Res. Lett. 36 (15), http://dx.doi.org/10.1029/2009GL039191.

Wojciech, M., 2018. Kriging method optimization for the process of DTM creation based on huge data sets obtained from MBESs. Geosciences 8 (12), 433. http://dx.doi.org/10.3390/geosciences8120433.

Worsley, D., 2008. The post-Caledonian development of Svalbard and the western Barents Sea. Polar Res. 27 (3), 298–317. http://dx.doi.org/10.1111/j.1751-8369.2008.00085.x.

Yoshikawa, K., 1998. The groundwater hydraulics of open system pingos. In: 7th International Permafrost Conference Yellowknife, Canada, Proceedings, p. 1177–1183.

Yoshikawa, K., Harada, K., 1995. Observations on nearshore pingo growth, Adventdalen, Spitsbergen. Permafr. Periglac. Process. 6 (4), 361–372. http://dx.doi.org/10.1002/ppp.3430060407.